POWER AND ENERGY FUTURE

Open Access
Research Article

Analysis and Suppression of Sending-End Transient Overvoltage in A Wind Power Integrated LCC-HVDC System under Commutation Failure

He Wang, Han Zhang, Jiajun Ma, Jing Bian, and Jiazhi Guo

***Abstract*—Receiving-end AC faults in line-commutated-converter-based high-voltage direct-current (LCC-HVDC) systems may trigger commutation failures (CFs) and cause sending-end transient overvoltage (TOV) during recovery. Existing work emphasizes rectifier reactive power control and DC current recovery, but the DC current undershoot from constant current controller over-regulation and its effect on sending-end TOV are not well studied. This paper analyzes the coupling among DC current, rectifier reactive consumption, AC filter reactive output, wind farm reactive response, and sending-end bus voltage during CFs. It reveals that the current undershoot reduces rectifier reactive consumption, aggravating the sending-end reactive surplus and elevating the peak TOV. A TOV assessment method incorporating the dynamic reactive response of wind farms is developed, along with a voltage-threshold-constrained DC current undershoot suppression strategy (VTC-DUS). The VTC-DUS calculates a current lower limit from a preset voltage threshold to form a modified DC current order, and adjusts the voltage-dependent current order limiter characteristic by the deviation between the modified and actual currents to suppress the excessive current drop. PSCAD/EMTDC simulations indicate that the peak TOV errors of the proposed method are below 0.01 pu for three-phase-to-ground faults and 0.03 pu for single-phase-to-ground faults, and that VTC-DUS effectively reduces the sending-end peak TOV under various fault conditions.**

***Index Terms*—Commutation failure, line-commutated-converter-based high-voltage direct-current (LCC-HVDC), wind power transmission, sending-end transient overvoltage, DC current undershoot.**

ABBREVIATION

LCC-HVDC	line-commutated-converter-based high-voltage direct-current
CFs	commutation failures
TOV	transient overvoltage
VTC-DUS	voltage-threshold-constrained DC current undershoot suppression strategy
RCFs	repetitive CFs
WTGs	wind turbine generators
VDCOL	voltage-dependent current order limiter
CCC	constant-current controller
DFIG	doubly fed induction generator
RSC	rotor-side converter
GSC	grid-side converter

Manuscript received 25 May, 2026; revised 20 September, 2026; accepted 24 September, 2026. Recommended by Associate Editor Qian Wei. *(Corresponding author: Jing Bian, e-mail: bj_jjj@163.com)*

J. Ma is with the Technology and Innovation Centre, Department of Electronic and Electrical Engineering, University of Strathclyde, 99 George Street, Glasgow, G1 1RD, UK.

H. Wang, H. Zhang, J. Bian and J. Guo are with School of Electrical Engineering, Northeast Electric Power University, Jilin 132012, China.

Color versions of one or more of the figures in this paper are available online at https://doi.org/10.26599/PEF.2026.9650018.

Digital Object Identifier 10.26599/PEF.2026.9650018

I. INTRODUCTION

In the context of the global shift toward low-carbon energy, the large-scale exploitation, grid integration, and long-distance delivery of renewable energy have emerged as a key trend in the evolution of future power systems [1]. Line-commutated-converter-based high-voltage direct-current (LCC-HVDC) transmission provides notable advantages, including ultra-high voltage levels, high power-transfer capability, and low transmission losses, making it a major technical solution for the long-distance transmission of renewable energy. However, the commutation process of LCC-HVDC is highly dependent on the AC-side voltage, rendering it prone to commutation failures (CFs) under receiving-end AC faults, and potentially inducing repetitive CFs (RCFs) during fault recovery. In the scenario where wind power is integrated and transmitted via LCC-HVDC, CFs not only affect DC power transfer but also cause a "low-then-high" transient voltage disturbance at the sending end, leading to sending-end transient overvoltage (TOV). In severe cases, this can trigger cascading disconnections of wind farms, significantly threatening grid security and stability.

Existing studies on sending-end TOV in LCC-HVDC systems under CFs mainly follow two research directions: quantitative assessment and suppression strategies.

In the area of quantitative TOV assessment, considerable work has covered aspects such as quantitative indices, peak value analytics, the influence of system strength, full-process

© The author(s) 2026. Published by Tsinghua University Press.
This is an open access article under the Creative Commons Attribution 4.0 International License (http://creativecommons.org/licenses/by/4.0/).

dynamic characterization, and assessment for renewable energy integration. To address the quantitative characterization of sending-end TOV, [2] proposed a quantitative overvoltage analysis method for ultra-high voltage direct current sending-end systems and compared the effects of different dynamic reactive power compensation devices on sending-end voltage recovery characteristics. Reference [3] derived an analytical expression for the peak TOV on the commutation bus caused by DC faults, enabling rapid TOV estimation based on AC system parameters and DC operating conditions. Reference [4] further derived an analytical relationship between the TOV and system strength indices, providing a theoretical basis for explaining overvoltage risks from the perspective of system strength. With respect to the full-process voltage disturbance at the sending end caused by CFs, [5] divided the transient voltage disturbance stages and revealed the evolutionary features of the voltage at the sending end, i.e., "low-then-high" and repetitive fluctuations. Reference [6] extended the TOV assessment to heterogeneous renewable energy integrated systems and established a TOV assessment method based on system strength analysis. Reference [7] examined the effects of various DC controller types and their parameter settings on the sending-end TOV. It also proposed a method for computing the sending-end transient voltage by deriving a simplified analytical formula for the DC current. Reference [8] constructed a dynamic phasor calculation method that accounts for the effects of CFs, providing model support for the calculation of large-disturbance transient responses.

In the area of TOV suppression strategies, existing studies mainly focus on HVDC reactive power control, wind farm side control, DC current control, and multi-objective coordinated control. In response to the voltage rise at the sending end following a sudden decrease in reactive power absorption at the rectifier station after CFs, [9] formulated the relationship between rectifier reactive power and DC voltage and current, and introduced a constant reactive power control method to maintain the transient reactive power consumption of the rectifier during the fault recovery stage and suppress the sending-end voltage rise. Reference [10] further considered the influence of signal delays on the entire transient voltage disturbance process and proposed an improved reactive power control method. For scenarios with high wind power penetration, [11] analyzed the impact of wind power control delays on sending-end TOV and proposed a delay compensation control strategy for wind turbine generators (WTGs). Regarding the influence of DC current variation on commutation security and fault recovery, [12] proposed a CF suppression method from the perspective of DC current prediction and control, demonstrating that the dynamic variation of the DC current significantly impacts the fault recovery process. Reference [13] proposed a DC current reference limitation method based on the sampled AC transient overvoltage, aiming to balance DC current recovery and sending-end overvoltage suppression. To address the problem that the conventional voltage-dependent current order limiter (VDCOL) may induce RCFs due to rapid DC current recovery, [14] proposed a multi-stage DC current control strategy to coordinate the relationships among TOV suppression, DC power recovery, and avoidance of RCFs. Reference [15] further considered the coupling relationship between sending-end TOV and RCFs, and proposed a control strategy that simultaneously suppresses TOV and RCFs.

The existing studies can be broadly divided into two categories: TOV assessment and TOV suppression. The former aims to quantify the sending-end voltage response under large disturbances, whereas the latter attempts to modify the HVDC or wind-farm control characteristics to mitigate the resulting overvoltage. These two research directions are closely related because an accurate assessment of the transient voltage and its dominant influencing variables provides the basis for designing an effective suppression strategy.

However, two related limitations remain. First, in many existing TOV assessment methods, the wind farm is represented by a constant or static reactive-power injection. Such a representation neglects the transient reactive-current responses of the rotor-side and grid-side converters and may therefore reduce the accuracy of the calculated sending-end voltage during the post-fault recovery process. Second, existing suppression strategies mainly focus on maintaining the rectifier reactive-power consumption, accelerating the DC-current recovery, or coordinating TOV suppression with the avoidance of RCFs. The excessive DC-current drop caused by the over-regulation of the rectifier constant-current controller (CCC) has not been systematically examined as an independent mechanism that aggravates the sending-end TOV.

These two limitations are intrinsically connected. An assessment model incorporating the dynamic wind-farm reactive-power response is required to determine the DC-current level corresponding to a prescribed voltage limit, whereas a targeted current-control mechanism is required to prevent the CCC-induced current undershoot from violating this voltage constraint. Therefore, this paper focuses on the "Analysis and Suppression of Sending-End Transient Overvoltage in a Wind Power Integrated LCC-HVDC System under Commutation Failure", and conducts a systematic study encompassing mechanism analysis, quantitative assessment, and suppression strategies. This study contributes in the following main aspects:

(1) The process by which the DC current undershoot caused by the over-regulation of the rectifier-side CCC aggravates the sending-end TOV is revealed. By analyzing the dynamic coupling relationships among the electrical quantities of the wind power integrated LCC-HVDC system during commutation failures, the pathway through which the excessive DC current drop reduces the reactive power consumption of the rectifier station, exacerbates the sending-end reactive power surplus, and elevates the peak TOV is clarified.

(2) A sending-end TOV assessment method that incorporates the dynamic reactive power response of the wind farm is established. By considering the coupling between wind turbine power output characteristics and the reactive interaction

at the rectifier station, a calculation method for the sending-end bus voltage is put forward.

(3) A voltage-threshold-constrained DC current undershoot suppression strategy (VTC-DUS) is proposed. On the one hand, the strategy employs the voltage assessment method that accounts for the dynamic reactive power response of the wind farm to calculate a DC current lower limit constrained by a preset voltage threshold, thereby generating a modified order. On the other hand, it adaptively adjusts the DC current according to the deviation between the modified order and the actual current. Through this coordinated mechanism, the strategy can not only effectively suppress the excessive current drop caused by CCC over-regulation, but also provide voltage-threshold-oriented suppression of the peak TOV under different fault conditions, achieving flexible, controllable, and efficient suppression of TOV.

The remainder of this paper is organized as follows. Section 2 describes the fundamental configuration of the LCC-HVDC system incorporating wind power. Section 3 conducts a quantitative analysis of the sending-end TOV and identifies its main influencing factors. Section 4 proposes the voltage-threshold-constrained DC current undershoot suppression strategy. Section 5 verifies and comparatively analyzes the proposed method through electromagnetic transient simulations. Section 6 concludes the paper.

II. Basic Structure of the LCC-HVDC Transmission System with Wind Power Integration

The equivalent impedance model of the wind power integrated LCC-HVDC system, which consists of the sending-end system, the rectifier station, the inverter station, and the receiving-end system, is shown in Fig. 1. The sending-end system includes WTGs, the sending-end AC system, and AC filters. In the figure, U_s is the terminal voltage of the WTG; U_w is the collector line voltage of the wind farm; U_{Lr} is the sending-end bus voltage; X_1 is the equivalent reactance between the wind farm and the rectifier station; X_2 is the equivalent reactance of the sending-end AC system; P_w and Q_w are the total active and reactive power output of the WTGs, respectively; P_{ac} and Q_{ac} are the active and reactive power fed into the DC system from the sending-end AC system, respectively; P_{dr} and Q_{dr} are the active power transmitted by the rectifier and the reactive power consumed by the rectifier, respectively; and Q_{cr} is the reactive power provided by the rectifier station filters and reactive power compensation devices.

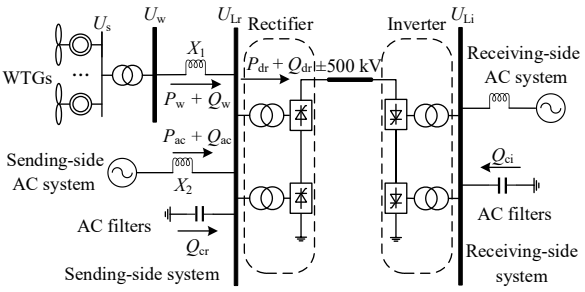

Fig. 1. Schematic diagram of the system structure of the wind power integrated LCC-HVDC system.

The configuration and aggregated representation of the wind farm are shown in Fig. 2. The wind farm is modeled using the detailed Type-III doubly fed induction generator (DFIG) benchmark model implemented in PSCAD/EMTDC [16]. Each WTG has a rated active power of 2 MW and a machine rating of 2.5 MVA. As shown in Fig. 2(a), the stator of the DFIG is directly connected to the grid, while the rotor is connected to the grid through the rotor-side converter (RSC) and the grid-side converter (GSC). In the figure, $P_{s,WTG}$ and $Q_{s,WTG}$ denote the active and reactive power output from the stator, respectively; and $P_{g,WTG}$ and $Q_{g,WTG}$ denote the active and reactive power output through the GSC, respectively.

As shown in Fig. 2(b), the wind farm consists of 300 identical WTGs. To avoid explicitly duplicating the switching devices and control systems of all units, one detailed Type-III WTG is combined with the standard PSCAD scaling component. The aggregation assumes that all WTGs have identical machine parameters, converter controls, wind-speed inputs, and terminal voltages. Under these homogeneous operating conditions, the wind-farm output current is expressed as $i_w = N_{WTG} i_{WTG}$, where i_{WTG} and i_w are the three-phase output-current vectors of the representative WTG and the aggregated wind farm, respectively, and N_{WTG} is the number of aggregated WTGs. Because all units are subjected to the same collector-bus voltage U_w, the wind-farm active and reactive powers are correspondingly obtained by scaling the outputs of the representative WTG. In this study, N_{WTG} = 300, resulting in a

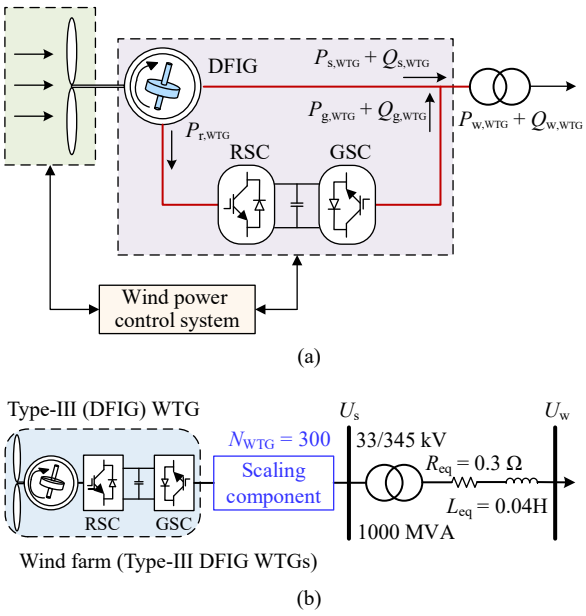

Fig. 2. Configuration and aggregated representation of the wind farm. (a) detailed Type-III DFIG structure of the representative WTG. (b) Wind-farm main-circuit and aggregation structure.

total rated active power of 600 MW and an aggregated machine capacity of 750 MVA.

The aggregated wind farm is connected to a 33 kV wind turbine terminal bus and subsequently integrated into the 345 kV wind farm cluster bus through a 1000 MVA and 33/345 kV step-up transformer. The electrical distance between the wind turbine terminal bus and the wind farm cluster bus is represented by an equivalent series branch with R_{eq} = 0.3 Ω and L_{eq} = 0.04 H. A uniform wind speed of 11 m/s is applied to all aggregated WTGs in the investigated cases.

The internal electromechanical, converter-control, and protection structures of the PSCAD benchmark model are used without modification. The official model documentation evaluates the dynamic performance of the detailed and average Type-III implementations under both wind-speed variations and a three-phase-to-ground fault. The documented comparisons show close agreement in the principal active-power, reactive-power, voltage, and post-fault recovery responses [16], [17], providing the validation basis for the WTG model adopted in this study.

The aggregation represents identical WTGs operating at the wind turbine terminal bus. Accordingly, differences in individual collector-feeder impedances, spatially nonuniform wind conditions, and wake effects within the wind farm are outside the scope of the present TOV analysis.

III. Mechanism Analysis of Sending-End Transient Overvoltage Caused by Commutation Failures

A. Characteristic analysis of the full transient process of commutation failures in a wind power integrated LCC-HVDC system

Before the stage-wise transient analysis, the commutation process is examined from the inverter-side currents in Fig. 3. Under normal operation, the six valves conduct sequentially, and the line-to-line commutation voltage drives the DC current from the outgoing valve to the incoming valve through the commutation inductance. Successful commutation requires the outgoing-valve current to decrease to zero before the commutation voltage reverses, while the incoming valve takes over the DC current.

After the receiving-end AC fault occurs at t = 2.0 s, the normal valve-conduction sequence in Fig. 3(a) is disrupted, and the regular six-step pattern of the converter-transformer valve-side currents in Fig. 3(b) collapses. The fault reduces and distorts the inverter-side commutation voltage, thereby decreasing the available commutation volt-second area. Meanwhile, Id increases transiently (Fig. 4(b)), increasing the current to be transferred within the available commutation interval. As a result, the outgoing-valve current cannot decrease to zero before voltage reversal, and the incoming valve cannot complete the current takeover. The resulting incomplete valve-to-valve current transfer and abnormal simultaneous valve conduction constitute the physical mechanism of CF. After fault

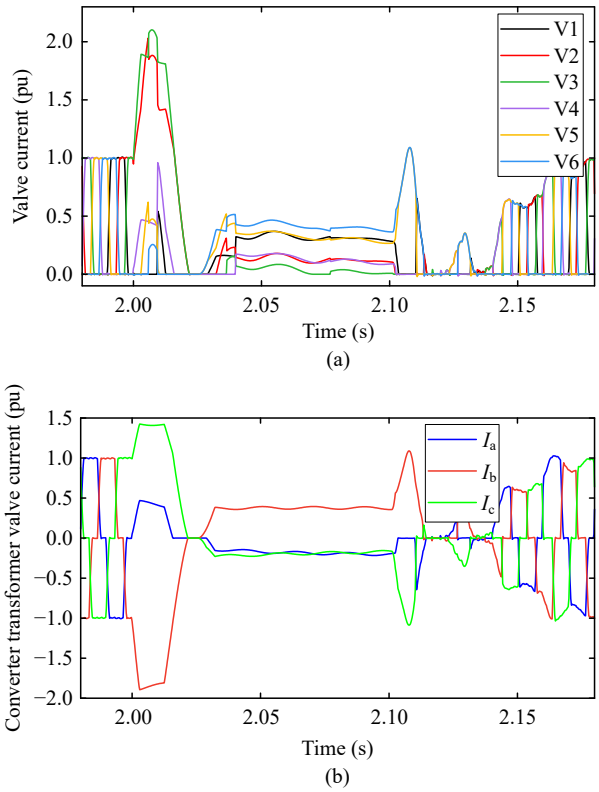

Fig. 3. Inverter-side current waveforms characterizing the commutation-failure process. (a) Valve currents of one 6-pulse bridge. (b) converter-transformer valve-side three-phase currents.

clearance, the valve-current sequence and valve-side current pattern gradually return to normal as commutation is restored.

According to the dynamic behavior of the extinction angle γ and DC current I_d, along with the main phases of fault progression, the transient process of commutation failures can be segmented into four distinct stages:

Stage I (fault duration period): From the occurrence of CFs to fault clearance. When a receiving-end AC fault occurs, U_{Li} and U_{di} simultaneously drop to zero (Fig. 4(d)), the commutation process is interrupted, and the processed extinction-angle signal decreases to zero (Fig. 4(a)). Affected by control delays and the rectifier-side CCC, I_d first rises and then drops (Fig. 4(b)). Since the reactive power consumed by the rectifier, Q_{dr}, is dominated by I_d and the firing angle α [18], the reactive power demand first increases and then decreases, and its waveform is highly coupled with that of I_d (Fig. 4(f)). The dynamic characteristics of Q_{dr} cause significant reactive power exchange near the sending-end bus, causing the sending-end bus voltage U_{Lr} to first decrease and then recover (Fig. 4(e)).

Stage II (waiting period): From fault clearance to the restoration of commutation. After fault clearance, U_{Li} rises rapidly; as the inverter has not yet recovered commutation, U_{di} follows U_{Li} with a slight increase and tends toward a fault steady state (Fig. 4(d)). Under VDCOL control, I_{dr_order} is maintained at the minimum output threshold I_{dmin} (Fig. 4(b)). I_d first undergoes a small steep increase as U_{di} rises rapidly,

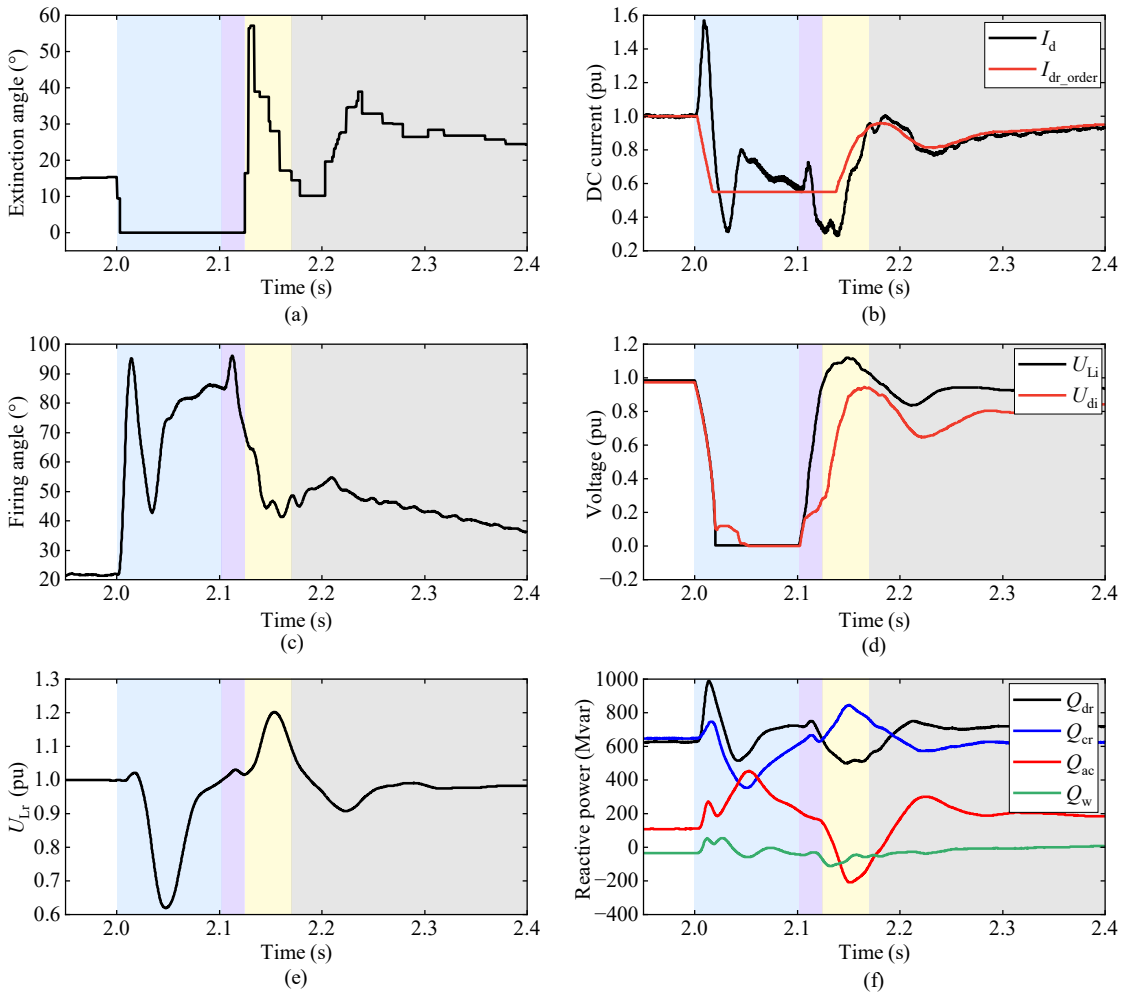

Fig. 4. Waveforms of electrical quantities during the transient process of commutation failures. (a) Inverter-side extinction angle γ. (b) DC current I_d and DC current order I_{dr_order}. (c) Rectifier-side firing angle α_r. (d) Receiving-end AC bus voltage U_{Li} and inverter-side DC voltage U_{di}. (e) Sending-end AC bus voltage U_{Lr}. (f) Reactive power consumed by the rectifier station Q_{dr}, reactive power provided by AC filters Q_{cr}, reactive power output from the sending-end AC system Q_{ac}, and reactive power output from the WTGs Q_w.

and then drops significantly under the effect of the firing angle α (Fig. 4(c)). After fault clearance, the inverter-side AC voltage starts to recover. However, normal commutation is not restored immediately, because the extinction margin remains insufficient for stable valve current transfer. Consequently, the system remains in a waiting state before entering the transient recovery stage.

Stage III (transient recovery period): From the restoration of commutation until the DC current recovers to near its initial value. The inverter resumes commutation, and U_{di} recovers rapidly (Fig. 4(d)). I_{dr_order} is first maintained at I_{dmin} and then rises linearly; during this period, I_d first oscillates slightly, then briefly decreases, and finally follows I_{dr_order} in rapid recovery (Fig. 4(b)). Affected by the combined effects of the delayed recovery of the VDCOL order, the voltage measurement delay, and the rapid regulation of the rectifier-side CCC, I_{dr_order} fails to follow the fast recovery of U_{di} in time, causing I_d to decrease again. This phenomenon is referred to in this paper as the CCC current undershoot effect. Under the influence of the decreasing firing angle α (Fig. 4(c)), Q_{dr} exhibits a downward trend (Fig. 4(f)). This drop in Q_{dr} leads to a surplus of reactive power at the sending-end bus, thereby elevating U_{Lr}. In response, the elevated U_{Lr} further drives up Q_{cr} considerably. Ultimately, under the coupled effects of Q_{dr}, Q_{cr}, Q_{ac}, and Q_w, Q_{ac} transitions from positive output to negative absorption (Fig. 4(f)). This process results in a large amount of reactive power flowing into the sending-end bus, and U_{Lr} reaches its peak value (Fig. 4(e)).

Stage IV (steady-state approaching period): The system gradually returns to steady-state operation, and I_d, Q_{dr}, Q_{cr}, and U_{Lr} all return to their pre-fault levels.

The extinction-angle waveform in Fig. 4(a) is the processed signal used by the control system rather than the instantaneous extinction angle of an individual commutation. In the PSCAD model, the measurement block outputs the minimum extinction angle over the most recent fundamental-frequency cycle and updates the signal every 30 electrical degrees. Therefore, a zero output over a certain interval means that a

zero extinction angle remains within the moving measurement window, rather than that the instantaneous extinction angle of every commutation remains continuously at zero.

Based on the above analysis of the transient response characteristics and co-evolution mechanism of the electrical quantities in the DC transmission system, the following conclusions can be drawn:

(1) During commutation failures, the sending-end bus voltage exhibits a "low-then-high" variation trend. This fluctuation essentially originates from the disruption and reconstruction of the dynamic balance among the reactive power consumed by the rectifier station, the reactive power provided by the AC filters, and the reactive power output from the sending-end AC system and the WTGs.

(2) The DC current is a key variable determining the TOV level. During fault recovery, a drop in the DC current reduces the reactive power consumption of the rectifier station, resulting in a reactive power surplus at the sending-end bus and thereby inducing TOV.

(3) During fault recovery, the CCC current undershoot effect further aggravates the TOV. Affected by the combined effects of the delayed recovery of the VDCOL order, the voltage measurement delay, and the rapid regulation of the rectifier-side CCC, the DC current drops excessively, which further reduces the reactive power consumption of the rectifier station, exacerbates the reactive power surplus, and ultimately elevates the peak TOV at the sending-end bus.

B. Calculation method of the sending-end bus voltage and analysis of influencing factors on TOV

Based on the analysis in Section 3.1, TOV typically occurs during the system recovery period after the first commutation failure, when the inverter side has resumed normal commutation. Therefore, quasi-steady-state equations can be used to describe the transient recovery process of the system.

B.1 Power characteristics of the sending-end system during faults

As shown in Fig. 1, when the system is in steady-state operation, the power balance between the sending-end system and the rectifier is maintained, which can be expressed by Eq. (1)

$$\begin{cases} P_{\mathrm{ac}} + P_{\mathrm{w}} = P_{\mathrm{dr}} \\ Q_{\mathrm{ac}} + Q_{\mathrm{cr}} + Q_{\mathrm{w}} = Q_{\mathrm{dr}} \end{cases} \tag{1}$$

For ease of analysis, the system in Fig. 1 is represented by its Thevenin equivalent, as shown in Fig. 5. In the figure, E_{r} is the equivalent voltage of the sending-end AC system, X_{eqr} is the equivalent reactance of the sending-end AC system, and ΔP and ΔQ are the net variations of the active and reactive power output from the sending-end AC system, respectively. Based on the power conservation principle, they can be expressed as

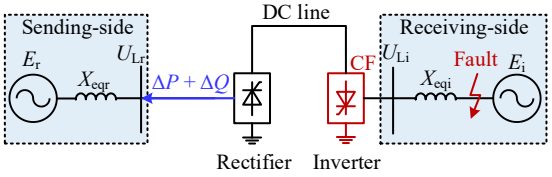

Fig. 5. Simplified equivalent circuit.

$$\begin{cases} \Delta P = P_{\mathrm{acN}} - P_{\mathrm{ac}} = P_{\mathrm{acN}} + P_{\mathrm{w}} - P_{\mathrm{dr}} \\ \Delta Q = Q_{\mathrm{acN}} - Q_{\mathrm{ac}} = Q_{\mathrm{acN}} + Q_{\mathrm{w}} + Q_{\mathrm{cr}} - Q_{\mathrm{dr}} \end{cases} \tag{2}$$

where P_{acN} and Q_{acN} are the active and reactive power output from the sending-end AC system during steady-state operation, respectively.

According to [5], the temporary change in Q_{dr} is the primary contributor to power imbalance and voltage deviations among interconnected systems, whereas the impact of Pdr is minor. Hence, the following analysis focuses solely on reactive power dynamics.

Following a commutation failure, the initial reactive power equilibrium at the sending end is disturbed: The reactive power absorbed by the rectifier, Q_{dr}, drops sharply, and the excess reactive power flows into the sending-end grid. Meanwhile, the reactive power output of the AC filters depends solely on the AC bus voltage; as the voltage rises, it further exacerbates the reactive power surplus. Although the WTGs can rapidly adjust their reactive power output according to the voltage, their regulation capacity is very small compared to the sudden drop in Q_{dr}. Consequently, the redundant reactive power is mainly injected into the sending-end AC system. The above power dynamic characteristics are consistent with the simulation results shown in Fig. 4(f).

Based on the LCC-HVDC quasi-steady-state model, the reactive power consumed by the rectifier can be obtained as

$$Q_{\mathrm{dr}} = I_{\mathrm{d}} \sqrt{U_{\mathrm{dr0}}^2 - U_{\mathrm{dr}}^2} \tag{3}$$

$$U_{\mathrm{dr0}} = \frac{3\sqrt{2}}{\pi} N K_{\mathrm{r}} U_{\mathrm{Lr}} \tag{4}$$

$$U_{\mathrm{dr}} = U_{\mathrm{di}} + R_{\mathrm{d}} I_{\mathrm{d}} + (L_{\mathrm{r}} + L_{\mathrm{d}} + L_{\mathrm{i}}) \frac{\mathrm{d}i}{\mathrm{d}t} \tag{5}$$

$$U_{\mathrm{di}} = \frac{3\sqrt{2}}{\pi} N K_{\mathrm{i}} U_{\mathrm{Li}} \cos\gamma - \frac{3}{\pi} \omega_{\mathrm{i}} L_{\mathrm{c}} I_{\mathrm{d}} \tag{6}$$

where U_{dr0} is the ideal no-load DC voltage at the rectifier side; U_{dr} and U_{di} are the DC voltages at the rectifier and inverter sides, respectively; N is the number of 6-pulse valve groups; K_{r} is the converter transformer ratio at the rectifier side; K_{i} is the converter transformer ratio at the inverter side; R_{d} and L_{d} are the equivalent resistance and equivalent inductance of the DC line, respectively; L_{r} and L_{i} are the smoothing reactor inductances at the rectifier and inverter sides, respectively; U_{Li} is the receiving-end AC bus voltage; ω_{i} is the angular fre-

清華大學出版社 Tsinghua University Press | SciOpen

quency of the receiving-end AC system; and L_c is the commutation inductance.

According to the operating characteristics of the LCC-HVDC system, the reactive power consumed by the rectifier accounts for approximately half of its output DC power [19]. To reduce line transmission losses, AC filters are usually configured at the converter station as local reactive power sources for on-site compensation. Their compensation capacity is proportional to the square of the bus voltage

$$Q_{cr} = Q_{crN}\left(\frac{U_{Lr}}{U_{LrN}}\right)^2 \tag{7}$$

Unlike conventional assessment methods that represent the wind farm as a constant reactive-power source, the proposed method updates the wind-farm reactive power at each calculation instant. Specifically, the stator reactive power and the grid-side-converter reactive power are calculated from the time-varying *dq*-axis voltage and current components, and their sum is used to determine Q_w. Consequently, the dynamic reactive-current responses of both the RSC and the GSC are incorporated into the sending-end reactive-power balance. This treatment enables the voltage-assessment model to account for the transient interaction between the wind farm and the sending-end AC system during the post-fault recovery process.

In the DFIG, the RSC and GSC regulate the rotor current and reactive current according to the power control loops, thereby controlling the stator-side output $Q_{s,WTG}$ and the GSC output $Q_{g,WTG}$

$$\begin{cases} Q_{s,WTG} = \dfrac{3}{2}(U_{sq}I_{sd} - U_{sd}I_{sq}) \\ Q_{g,WTG} = \dfrac{3}{2}(U_{sq}I_{gd} - U_{sd}I_{gq}) \end{cases} \tag{8}$$

where U_{sd} and U_{sq} are the *d*-axis and *q*-axis components of the terminal voltage, respectively; I_{sd} and I_{sq} are the *d*-axis and *q*-axis components of the stator current, respectively; and I_{gd} and I_{gq} are the *d*-axis and *q*-axis components of the GSC current, respectively.

Based on the power flow shown in Fig. 2(a), the reactive power output from the WTG, $Q_{w,WTG}$, is composed of both $Q_{s,WTG}$ and $Q_{g,WTG}$. When the DFIG adopts stator-voltage-oriented vector control, $U_{sd} = U_s$, $U_{sq} = 0$, and therefore Q_w can be expressed as:

$$Q_w = -\frac{3}{2}N_{WTG}U_s\left(i_{gq} + i_{sq}\right) \tag{9}$$

Based on Figs. 1 and 5, the voltage drop caused by X_1, ΔU_w, can be expressed as

$$\Delta U_w = U_w - U_{Lr} = \frac{(Q_w - \Delta Q_w)X_1}{U_{Lr}} \tag{10}$$

The surplus reactive power flowing into the WTGs, ΔQ_w, can be calculated as

$$\Delta Q_w = \frac{X_1}{X_1 + X_2}\Delta Q \tag{11}$$

By combining the WTG transformer ratio $K_w = U_{Lr}/U_s$, the following is derived

$$U_w = \frac{K_w\left(U_{Lr}^2 - \dfrac{X_1^2}{X_1 + X_2}\Delta Q\right)}{U_{Lr}K_w + \dfrac{3}{2}X_1N_{WTG}\left(i_{gq} + i_{sq}\right)} \tag{12}$$

Taking the system base capacity as 1000 MVA, short-circuit ratio (SCR) = 3, U_{LrN} = 345 kV, and the total reactance $X_1 + X_2$ = 39.675 Ω, and setting ΔQ = 0.2 pu, $i_{gq} + i_{sq}$ = 0.5 pu, and K_w = 10, the relationship curve between X_1 and U_w is obtained, as depicted in Fig. 6, where U_w decreases with the increase of X_1. When X_1 approaches 0, $U_w = U_{Lr}$ = 1.18 pu; at this point, the risk of WTG high-voltage disconnection is greatest. Therefore, X_1 = 0 is taken as the extreme operating condition in the subsequent analysis.

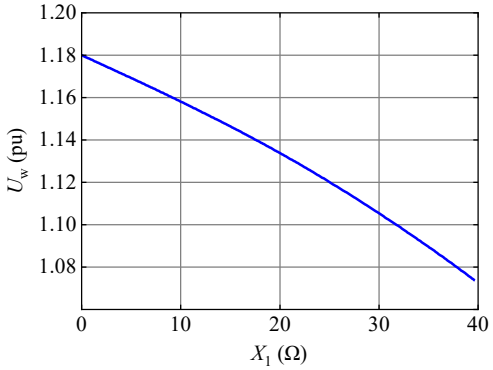

Fig. 6. Relationship curve between X_1 and U_w.

It should be emphasized that X_1 = 0 is not intended to represent a physical collector system with zero impedance. Instead, it denotes a limiting condition in which the wind-farm collector bus is electrically close to the sending-end converter bus. Under the reactive-power-flow direction considered during stage III, $Q_w - \Delta Q_w$ is positive, and Eq. (10) gives $\partial\Delta U_w/\partial X_1 > 0$. Therefore, a reduction in X_1 decreases the voltage drop between the two buses and increases U_w. When X_1 approaches zero, U_w approaches U_{Lr}, and the sending-end overvoltage is transferred to the wind-farm collector bus without attenuation. Accordingly, X_1 = 0 provides a conservative boundary condition for evaluating the wind-turbine overvoltage risk.

B.2 Calculation method of the sending-end bus voltage

The following assumptions are adopted to derive the sending-end bus-voltage expression. First, the derivation is applied to the post-fault recovery stage after normal inverter commutation has been restored, during which the system can be described using fundamental-frequency quasi-steady-state equations. Second, based on Fig. 5, the sending-end AC sys-

tem is represented by a Thevenin equivalent voltage source. Third, because the sending-end voltage deviation is mainly determined by the reactive-power imbalance during this stage, the contribution of the active-power variation to the voltage magnitude is neglected. Fourth, the reactive power supplied by the AC filters is assumed to be proportional to the square of the sending-end bus voltage. Finally, stator-voltage-oriented control is adopted for the DFIG, and the conservative limiting condition $X_1 = 0$ is used, such that $U_w = U_{Lr}$ and $U_s = U_{Lr}/K_w$. U_{Lr} can be approximated as

$$U_{Lr} = U_{LrN} + \frac{\Delta Q X_{eqr}}{U_{LrN}} \tag{13}$$

Substituting $X_1 = 0$ (i.e., $U_w = U_{Lr}$) and Eqs. (7) and (9) into Eq. (2), ΔQ can be expressed as

$$\Delta Q = Q_{acN} - \frac{3}{2}\cdot\frac{U_{Lr}}{K_w}N_{WTG}\left(i_{gq}+i_{sq}\right) + \frac{U_{Lr}^2}{U_{LrN}^2}Q_{crN} - Q_{dr} \tag{14}$$

Substituting Eq. (14) into Eq. (13), we obtain

$$U_{Lr} = U_{LrN} + \frac{X_{eqr}}{U_{LrN}}\left[Q_{acN} - \frac{3U_{Lr}}{2K_w}\left(i_{gq}+i_{sq}\right) + \frac{U_{Lr}^2}{U_{LrN}^2}Q_{crN} - Q_{dr}\right] \tag{15}$$

Rearranging the terms yields

$$aU_{Lr}^2 + bU_{Lr} + c = 0 \tag{16}$$

where

$$a = \frac{X_{eqr}Q_{crN}}{U_{LrN}^3} \tag{17}$$

$$b = -\left(1 + \frac{3X_{eqr}}{2U_{LrN}K_w}N_{WTG}\left(i_{gq}+i_{sq}\right)\right) \tag{18}$$

$$c = U_{LrN} + \frac{X_{eqr}}{U_{LrN}}\left(Q_{acN} - Q_{dr}\right) \tag{19}$$

Hence

$$U_{Lr} = \frac{-b - \sqrt{b^2 - 4ac}}{2a} \tag{20}$$

B.3 Influencing factors of sending-end bus TOV

To further analyze the influencing factors of TOV, Eqs. (2), (7), and (13) are substituted into Eq. (3), yielding Eq. (21)

$$I_d = \frac{Q_{acN} + Q_w + \frac{U_{Lr}^2}{U_{LrN}^2}Q_{crN} - \frac{(U_{Lr}-U_{LrN})U_{LrN}}{X_{eqr}}}{\sqrt{U_{dr0}^2 - U_{dr}^2}} \tag{21}$$

From Section 3.1, it can be seen that the TOV peak occurs in stage III of Fig. 4. In this stage, $U_{Li}\cos\gamma$ increases monotonically with time, while the variations of Q_w and the DC current change rate di/dt are very small and can be approximated as constant. At this point, Eq. (21) involves only three variables: I_d, U_{Lr}, and $U_{Li}\cos\gamma$. The quantitative relationship among them is shown in Fig. 7.

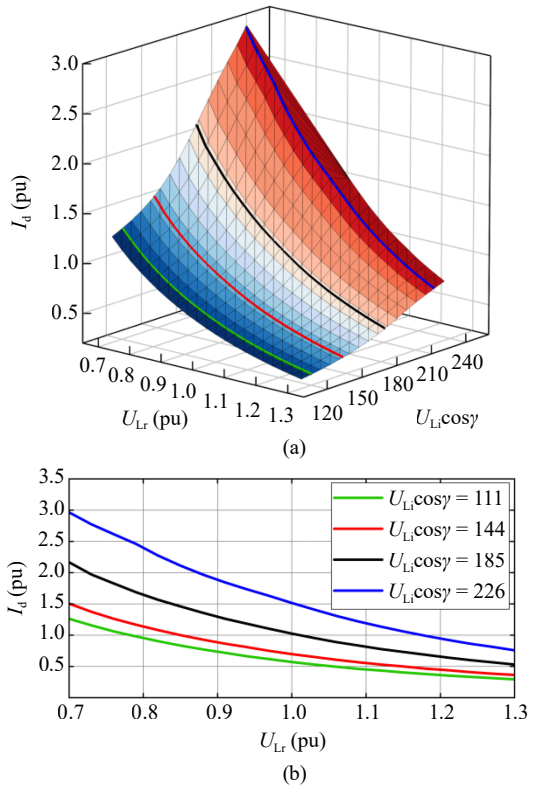

Fig. 7. Quantitative relationship between DC current and sending-end bus voltage. (a) Three-dimensional (3D) surface plot (b) 3D front view.

As shown in Fig. 7, for all values of $U_{Li}\cos\gamma$, U_{Lr} increases monotonically as I_d decreases. It can be inferred that, under the studied recovery-stage operating conditions, the excessive drop of I_d is a major factor aggravating the increase in U_{Lr}. Therefore, this paper will proceed from the DC current regulation to design a corresponding control strategy.

IV. Proposed VTC-DUS

CCC, as a fast control link for suppressing commutation failures, produces a current undershoot effect that is a negative consequence of the control link itself. This effect has not been systematically considered and compensated for in the design of existing suppression strategies, which may weaken their actual performance.

To address this issue, this paper proposes the VTC-DUS. The strategy first calculates a DC current lower limit in real time constrained by a fixed voltage threshold, and combines it with the conventional VDCOL output to generate a modified order, I_{dr_corr}. Then, based on the deviation between I_{dr_corr} and the actual current, it drives the adaptive shift of the VDCOL characteristic, so that the current order is moderately elevated while maintaining a gradual variation characteristic.

A. Control and measurement dynamics of the benchmark HVDC system

HVDC control system integrated with the proposed VTC-DUS shown in Fig. 8 is developed from the PSCAD Monopole HVDC Transmission System CIGRE Benchmark model. The rectifier operates under constant-current control, whereas the inverter employs coordinated constant-current control, constant-extinction-angle control, voltage-dependent current-order limitation, and current-error control.

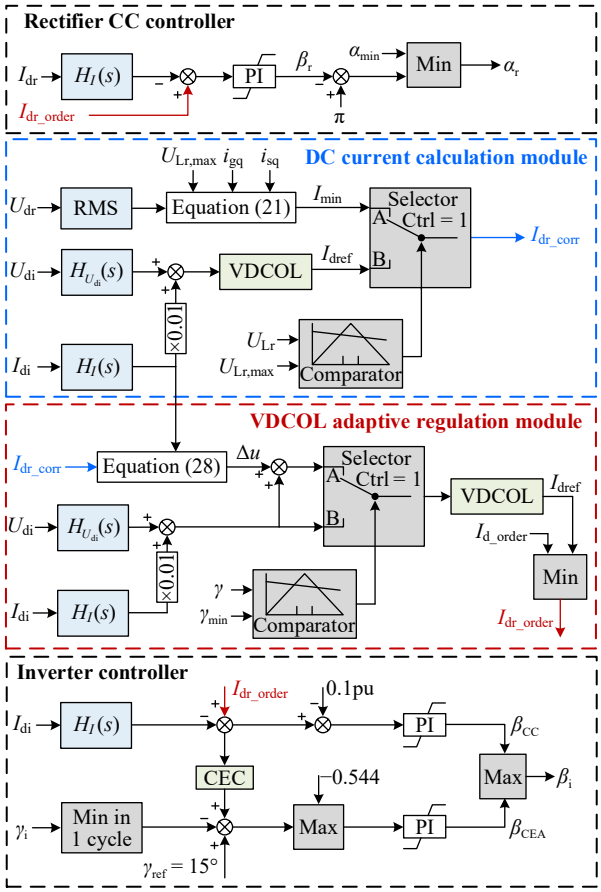

Fig. 8. HVDC control system integrated with the proposed VTC-DUS.

The rectifier CCC regulates the advance-angle order according to the deviation between the final current order and the measured DC current. The corresponding control relationship is expressed as

$$\alpha_{\mathrm{r}} = \pi - K_{\mathrm{p}}\left(I_{\mathrm{dr_order}} - I_{\mathrm{dr}}\right) + T_{\mathrm{i}}\int\left(I_{\mathrm{dr_order}} - I_{\mathrm{dr}}\right)\mathrm{d}t \tag{22}$$

where α_{r} is the firing angle of the rectifier; K_{p} and T_{i} are the proportional gain and integral time constant of the CCC, respectively; I_{dr} is the measured DC current on the rectifier side; and $I_{\mathrm{dr_order}}$ is the final DC current order.

The VDCOL reduces the DC-current order during a DC-voltage depression and restores the current order gradually as the inverter-side DC voltage recovers. Based on the filtered inverter-side DC voltage U_{di}, the conventional VDCOL characteristic is expressed as

$$I_{\mathrm{dref}} = \begin{cases} I_{\mathrm{dmin}}, & U_{\mathrm{di}} \le U_{\mathrm{L}} \\ I_{\mathrm{dmin}} + \dfrac{I_{\mathrm{dmax}} - I_{\mathrm{dmin}}}{U_{\mathrm{H}} - U_{\mathrm{L}}}\left(U_{\mathrm{di}} - U_{\mathrm{L}}\right), & U_{\mathrm{L}} < U_{\mathrm{di}} \le U_{\mathrm{H}} \\ I_{\mathrm{dmax}}, & U_{\mathrm{di}} > U_{\mathrm{H}} \end{cases} \tag{23}$$

where I_{dmin} and I_{dmax} are the lower and upper limits of the VDCOL output, and U_{L} and U_{H} are the lower and upper DC-voltage thresholds, respectively. The parameters adopted from the CIGRE benchmark model are I_{dmin} = 0.55 pu, I_{dmax} = 1.0 pu, U_{L} = 0.4 pu, and U_{H} = 0.9 pu. The VDCOL is implemented as a static piecewise mapping and therefore introduces no independent dynamic lag. Its effective response is mainly determined by the measurement dynamics of U_{di}.

At the inverter, the constant-current controller and the constant-extinction-angle controller (PI) coordinate the DC-current and commutation-margin regulation. Their proportional gains and integral time constants are $K_{\mathrm{p,CC}}$ = 0.63 and $T_{\mathrm{i,CC}}$ = 0.01524 s for the current controller, and $K_{\mathrm{p,CEA}}$ = 0.7506 and $T_{\mathrm{i,CEA}}$ = 0.0544 s for the extinction-angle controller. The CEC provides a bounded nonlinear correction according to its current-deviation input, thereby supporting the coordination between the inverter current-control and extinction-angle-control branches.

In the adopted benchmark model, the CEC is implemented using an up-ramp transfer function. Denoting its current-deviation input and output correction signal by e_{CEC} and y_{CEC}, respectively, its characteristic is

$$y_{\mathrm{CEC}} = \begin{cases} 0, & e_{\mathrm{CEC}} \le 0 \\ 2.793 e_{\mathrm{CEC}}, & 0 < e_{\mathrm{CEC}} < 0.1 \\ 0.2793, & e_{\mathrm{CEC}} \ge 0.1 \end{cases} \tag{24}$$

where e_{CEC} is the current-deviation signal applied to the CEC and y_{CEC} is the corresponding bounded correction signal. Since the CEC is implemented as a static up-ramp mapping rather than a time-domain ramp generator, it does not introduce an additional time constant or intentional control delay.

The measurement and signal-processing dynamics retained in the electromagnetic transient model are summarized in Table 1. The rectifier-side and inverter-side DC currents are processed by identical first-order transducers, whereas the inverter-side DC voltage is processed by a slower first-order voltage transducer

$$\begin{cases} H_I(s) = \dfrac{0.5}{1 + 0.0012s} \\ H_{U_{\mathrm{di}}}(s) = \dfrac{0.002}{1 + 0.02s} \end{cases} \tag{25}$$

The sending-end AC-bus voltage U_{Lr} and the rectifier-side DC voltage U_{dr}, used by the DC current calculation module,

TABLE 1
MEASUREMENT AND CONTROL DYNAMICS OF THE HVDC SYSTEM

Function	Transfer function or logic	Parameters	Dynamic characteristic
I_{dr}	$0.5/(1+0.0012s)$	$G=0.5$, $T=1.2$ ms	$t_{95}\approx 3.6$ ms
I_{di}	$0.5/(1+0.0012s)$	$G=0.5$, $T=1.2$ ms	$t_{95}\approx 3.6$ ms
U_{di}	$0.002/(1+0.02s)$	$G=0.002$, $T=20$ ms	$t_{95}\approx 60$ ms
U_{dr}/U_{Lr}	Digital RMS calculation	$T_w=20$ ms	Updated every $\Delta t=50$ μs
γ	One-cycle moving minimum	$T_{w,\gamma}=20$ ms	Updated every $\Delta t=1.667$ ms
Rectifier CCC	PI	$K_p=1.0989$, $T_i=0.01392$ s	—
Inverter CC	PI	$K_p=0.63$, $T_i=0.01524$ s	—
Inverter CEA	PI	$K_p=0.7506$, $T_i=0.0544$ s	—

are obtained through the digital three-phase root-mean-square (RMS) voltage measurement in PSCAD. The proposed VTC-DUS uses the RMS value of the converter AC-bus voltage rather than the instantaneous voltage waveform for voltage-threshold constraint calculation. This measurement calculates the RMS value using a moving data window that spans one fundamental-frequency cycle. At a system frequency of 50 Hz, the window length is 20 ms, and the RMS output is refreshed at every EMTDC solution step. Therefore, the inherent calculation delay introduced by the RMS measurement is included in the control response of the proposed strategy.

The extinction-angle signal used for control is not the instantaneous value associated with a single commutation. The measured extinction angle is processed by a one-cycle minimum-value function, which outputs the minimum value over the most recent fundamental-frequency cycle and updates the output every 30 electrical degrees. At 50 Hz, the moving-window length and update interval are 20 and 1.667 ms, respectively. This processing prevents the adaptive VDCOL from being enabled immediately after an isolated temporary recovery of the extinction angle.

For the first-order measurement functions, t_{95} denotes the time required for the step response to reach 95% of its final value, which is approximately three times the corresponding time constant.

During a receiving-end voltage depression following a commutation failure, the filtered inverter-side DC voltage U_{di} first reduces the conventional VDCOL current order. The sending-end digital RMS voltage U_{Lr} is simultaneously compared with the prescribed voltage threshold. When U_{Lr} exceeds $U_{Lr,max}$, the DC-current calculation module determines the current lower limit corresponding to the voltage constraint and generates the modified current order. During the commutation-failure interval, the adaptive VDCOL regulation remains disabled. It is enabled only after the one-cycle minimum extinction-angle signal γ recovers above γ_{min}, thereby avoiding premature current-order elevation before stable commutation recovery. The corrected current order is subsequently tracked by the rectifier CCC. Consequently, the response sequence of VTC-DUS is governed by voltage-threshold detection, current-limit calculation, commutation-recovery confirmation, adaptive VDCOL adjustment, and CCC current tracking.

B. DC current calculation module based on voltage threshold constraint

As shown in Fig. 8, the strategy consists of two core modules: a DC current calculation module based on a voltage threshold constraint, and a VDCOL adaptive regulation module based on current order deviation.

This paper assumes that the terminal voltage threshold that leads to WTG high-voltage disconnection is $U_{s,max}$. When U_s exceeds $U_{s,max}$, the WTG is disconnected. Under the extreme operating condition of $X_1=0$, the collector line voltage of the wind farm $U_w=U_{Lr}$. Considering the WTG transformer ratio K_w, the WTG terminal voltage U_s can therefore be indirectly constrained by limiting U_{Lr}.

The switching criterion of the DC current calculation module is

$$U_{Lr}\geq U_{Lr,max} \tag{26}$$

where $U_{Lr,max}$ is the preset voltage threshold, and its value can be adjusted to suit different systems and practical needs.

When U_{Lr} exceeds $U_{Lr,max}$, the sending end is exposed to TOV risk. Under such conditions, raising the DC current command I_{dr_order} helps enhance the reactive power drawn by the rectifier station, thereby alleviating the reactive power surplus at the sending end.

As shown in Fig. 8, the system detects the value of U_{Lr} in real time. When the voltage exceeds the preset value, the two-input selector switches from B to A, and the current lower limit I_{min} calculated based on $U_{Lr,max}$ is selected as the output. Otherwise, the original VDCOL order I_{dref} is output, and the modified order I_{dr_corr} is finally generated.

According to Eq. (21), I_{min} can be calculated by

$$I_{min}=\frac{Q_{acN}-\frac{3U_{Lr}}{2K_w}N_{WTG}\left(i_{gq}+i_{sq}\right)+\frac{U_{Lr}^2}{U_{LrN}^2}Q_{crN}-\frac{(U_{Lr}-U_{LrN})U_{LrN}}{X_{eqr}}}{\sqrt{\left(\frac{3\sqrt{2}}{\pi}NKU_{Lr}\right)^2-U_{dr}^2}} \tag{27}$$

The preset voltage threshold $U_{Lr,max}$ is substituted into Eq. (27) as U_{Lr} for the calculation, while the other variables (i_{gq},

清華大學出版社 Tsinghua University Press | SciOpen

i_{sq}, and U_{dr}) adopt their real-time measured values to ensure calculation accuracy.

C. VDCOL adaptive regulation module based on current order deviation

As shown in Fig. 9(a), a real-time deviation Δi exists between the modified order I_{dr_corr} and the actual inverter-side current I_{di}. This deviation quantitatively characterizes the extent to which the current operating point deviates from the desired current recovery path, and also reflects the amplitude of the additional current increase required by the system to suppress TOV. As shown in Fig. 9(b), to actively elevate the current order, the real-time deviation Δi is mapped to a horizontal offset Δu of the VDCOL characteristic curve without changing its slope

$$\begin{cases} \Delta i = I_{dr_corr} - I_{di} \\ \Delta u = \left(I_{dr_corr} - I_{di}\right) \dfrac{U_H - U_L}{I_{dmax} - I_{dmin}} \end{cases} \tag{28}$$

where I_{dmin} and I_{dmax} represent the minimum and maximum values of I_{dref}, and U_L and U_H represent the minimum and maximum threshold voltages of U_{di}, respectively.

From the analysis in Section 3.1, it is evident that after the system enters stage III, the CCC current undershoot effect causes an excessive drop in I_d. Therefore, the switching criterion of the VDCOL adaptive regulation module is set as

$$\gamma \geq \gamma_{min} \tag{29}$$

As shown in Fig. 8, the system detects the value of γ in real time and compares it with the critical extinction angle γ_{min} (usually set to 7°) to determine the occurrence and recovery of commutation failures. When $\gamma < \gamma_{min}$, the system is in a commutation failure state, the two-input selector outputs signal B, and the VDCOL control operates in mode 1, as shown in Fig. 9(b). Following the occurrence of a commutation failure, when γ subsequently recovers to $\gamma \geq \gamma_{min}$, the inverter is considered to have resumed normal commutation and the system enters stage III. The selector is then latched to signal A, and the VDCOL switches from mode 1 to mode 2. In mode 2, the DC-current order is adaptively elevated according to the real-time current-order deviation. Thereafter, the selector maintains the A signal output state until the next commutation failure event occurs.

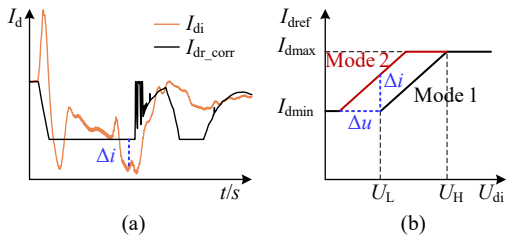

Fig. 9. Mapping relationship between current order deviation and VDCOL horizontal offset. (a) Tracking curves of I_d and I_{dr_corr}. (b) Improved VDCOL characteristic curve.

As Δi gradually decreases with system recovery, Δu can automatically decay to zero, and the VDCOL characteristic can return to its original position. Therefore, this module only needs to be activated in stage III without requiring an explicit exit mechanism, allowing the system to adaptively return to steady state.

D. Online implementation of VTC-DUS

The proposed VTC-DUS is implemented as a measurement-driven control scheme and does not require prior knowledge of the fault inception time, fault clearing time, or fault type. The fault categories adopted in the subsequent electromagnetic transient simulations are used only to define the test conditions and are not input signals of the controller. The implementation of VTC-DUS relies on the measured and filtered electrical quantities shown in Fig. 8 rather than on an externally provided fault command.

The two control conditions perform complementary functions. The sending-end voltage condition determines whether the additional DC-current lower limit calculated in Section 4.2 is required, whereas the commutation-state condition described in Section 4.3 determines whether the adaptive VDCOL regulation can be enabled. Thus, the voltage-threshold module responds to the measured TOV risk, while the VDCOL adaptive-regulation module is activated only after the inverter has recovered from commutation failure. Neither condition requires identification of the initiating AC-fault category.

It should be noted that the proposed VTC-DUS does not require additional communication signals between the sending-end and receiving-end converters. The required electrical quantities are obtained from the existing HVDC measurement and control system. The conventional VDCOL in the CIGRE HVDC benchmark model is retained before and after applying VTC-DUS, and no additional enable or disable delay is introduced. Therefore, the inherent measurement and control delays in the original HVDC system are preserved in the EMTDC simulation. The proposed strategy does not directly compensate for these inherent delays. Instead, it suppresses the excessive DC-current undershoot caused by the delayed recovery of the current order, thereby mitigating the adverse impact of these delays on the sending-end transient overvoltage.

To further clarify the dynamic response of VTC-DUS under practical HVDC control conditions, the timing relationship among U_{Lr}, U_{di}, I_d, I_{dr_order}, and the activation signals of two modules is illustrated in Fig. 10. After fault clearance, U_{di} gradually recovers, whereas the recovery of I_{dr_order} is delayed by the inherent dynamics of the HVDC control system, resulting in further DC-current reduction under CCC regulation. The DC current calculation module and VDCOL adaptive regulation module are activated at t_{act1} and t_{act2}, respectively. Since both activation time occurs before the minimum DC current point t_{min}, the proposed strategy can effectively suppress excessive DC-current undershoot under practical control dynamics.

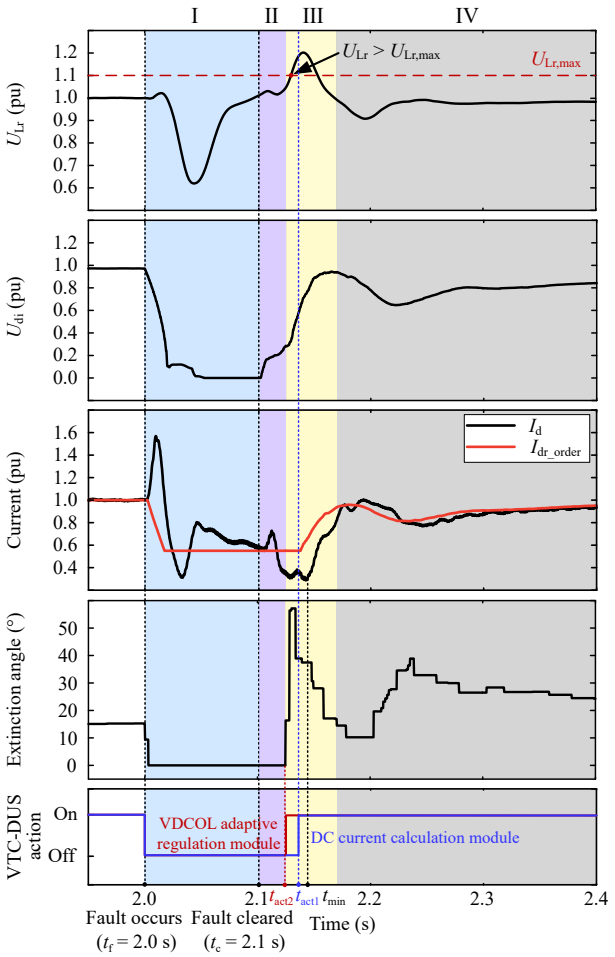

Fig. 10. Timing relationship among voltage recovery, current-order response, and VTC-DUS activation.

V. Simulation Validation

To validate the accuracy of the proposed TOV assessment method and the effectiveness of the VTC-DUS, a wind power integrated LCC-HVDC system, as shown in Fig. 1, is built in PSCAD/EMTDC. The detailed parameters are provided in Table 2.

A. Simulation analysis of the TOV assessment method

The proposed TOV assessment method is based on quasi-steady-state equations and is applicable to the transient recovery period (stage III) and the steady-state approaching period (stage IV), during which the inverter has resumed normal commutation. Therefore, this section only validates the accuracy of the equations in these two stages.

Three-phase-to-ground and single-phase-to-ground inductive faults at the receiving-end AC bus are used as test cases. The fault is applied at 2 s and lasts for 0.1 s. The simulation and calculation results of the sending-end bus voltage U_{Lr} are shown in Figs. 11 and 12.

This paper establishes two simplified methods for comparison: Method 1 disregards the dynamic reactive power exchange between the wind farm and the AC grid, treating Q_w as the constant rated reactive power Q_{wN} under steady-state conditions [9]. Method 2 omits the transient component of U_{dr} in Q_{dr} calculations and approximates U_{dr} by its rated value U_{drN} at the rectifier side [7]. A comparison of the calculation

TABLE 2
Simulation Data of LCC-HVDC and DFIG

Item	Symbol	Parameter	Value
LCC-HVDC	P_{dc}	Rated power	1000 MW
	U_{dc}	Rated DC voltage	500 kV
	I_{dc}	Rated DC current	2 kA
	Q_{cr}	Rectifier VAR compensator	643 Mvar
	SCR_s	Sending-end system short-circuit ratio	2.5
	SCR_r	Receiving-end system short-circuit ratio	2.5
DFIG	P_w	Rated power	2 MW × 300
	U_s	Rated stator voltage	690 V
	L_{ls}	Stator leakage inductance	0.173 pu
	L_{lr}	Rotor leakage inductance	0.16 pu
	L_m	Mutual inductance	2.78 pu

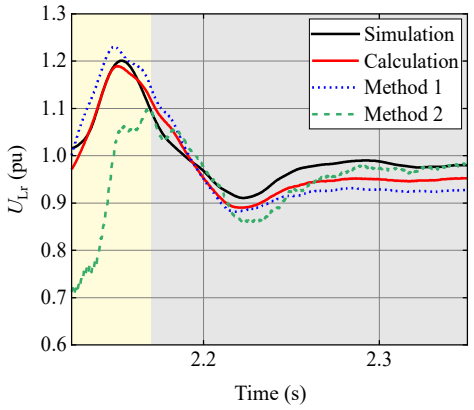

Fig. 11. Simulation and calculation results under a three-phase-to-ground fault.

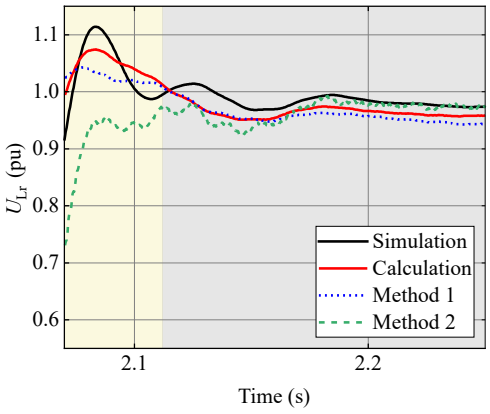

Fig. 12. Simulation and calculation results under a single-phase-to-ground fault.

results of the three methods in Figs. 11 and 12 shows that the calculation accuracy of the proposed TOV assessment method is significantly better than that of methods 1 and 2 under both three-phase and single-phase inductive-to-ground faults.

The fundamental difference between method 1 and the proposed method lies in the treatment of the wind-farm reactive power. Method 1 assumes that Q_w remains equal to its steady-state value and therefore neglects the transient reactive-current responses of the RSC and GSC. In contrast, the proposed method updates Q_w using the instantaneous dq-axis quantities in Eqs. (8) and (9). The improved agreement with the electromagnetic transient simulation confirms that the dynamic wind-farm reactive-power response cannot be neglected when assessing the sending-end TOV.

The voltage assessment method proposed in this paper exhibits high calculation accuracy under three-phase-to-ground inductive faults, with a peak TOV error of less than 0.01 pu; whereas under single-phase-to-ground inductive faults, the error is relatively larger, with a peak TOV error of less than 0.03 pu. This difference is mainly determined by the fault symmetry. During a three-phase fault, the commutation process on the inverter side is symmetrical, and the variations of the electrical quantities are consistent with the quasi-steady-state assumption, thus resulting in higher calculation accuracy.

B. Simulation analysis of the control strategy

A control system model, illustrated in Fig. 8, is implemented in PSCAD using the standard control strategy of the CIGRE HVDC benchmark model. The static voltage threshold $U_{Lr,max}$ is configured as 1.1 pu. Under different grid fault conditions, including three-phase-to-ground (TPG), single-phase-to-ground (SPG), double-line-to-ground (LLG), and line-to-line (LL) faults, the proposed strategy is compared with the original control. The cases are listed in Table 3.

TABLE 3
CASE CONDITIONS

Cases	Fault type	Fault inductance L_f (H)	Fault duration t_f (s)	Figs
A	TPG	0.001	0.1	Fig.13(A)
B	TPG	0.001	0.125	Fig.13(B)
C	TPG	0.001	0.15	Fig.13(C)
D	TPG	0.0001	0.1	Fig.14(D)
E	TPG	0.01	0.1	Fig.14(E)
F	TPG	1	0.1	Fig.14(F)
G	SPG	0.001	0.1	Fig.15(G)
H	LLG	0.001	0.1	Fig.15(H)
I	LL	0.001	0.1	Fig.15(I)

Cases A–C vary the fault duration, cases D–F vary the fault inductance, and cases G–I consider different fault types. For the same cases, the processed extinction-angle signal γ in Figs. 13–15 describes the loss and recovery of the commutation margin, while the converter-transformer valve-side currents

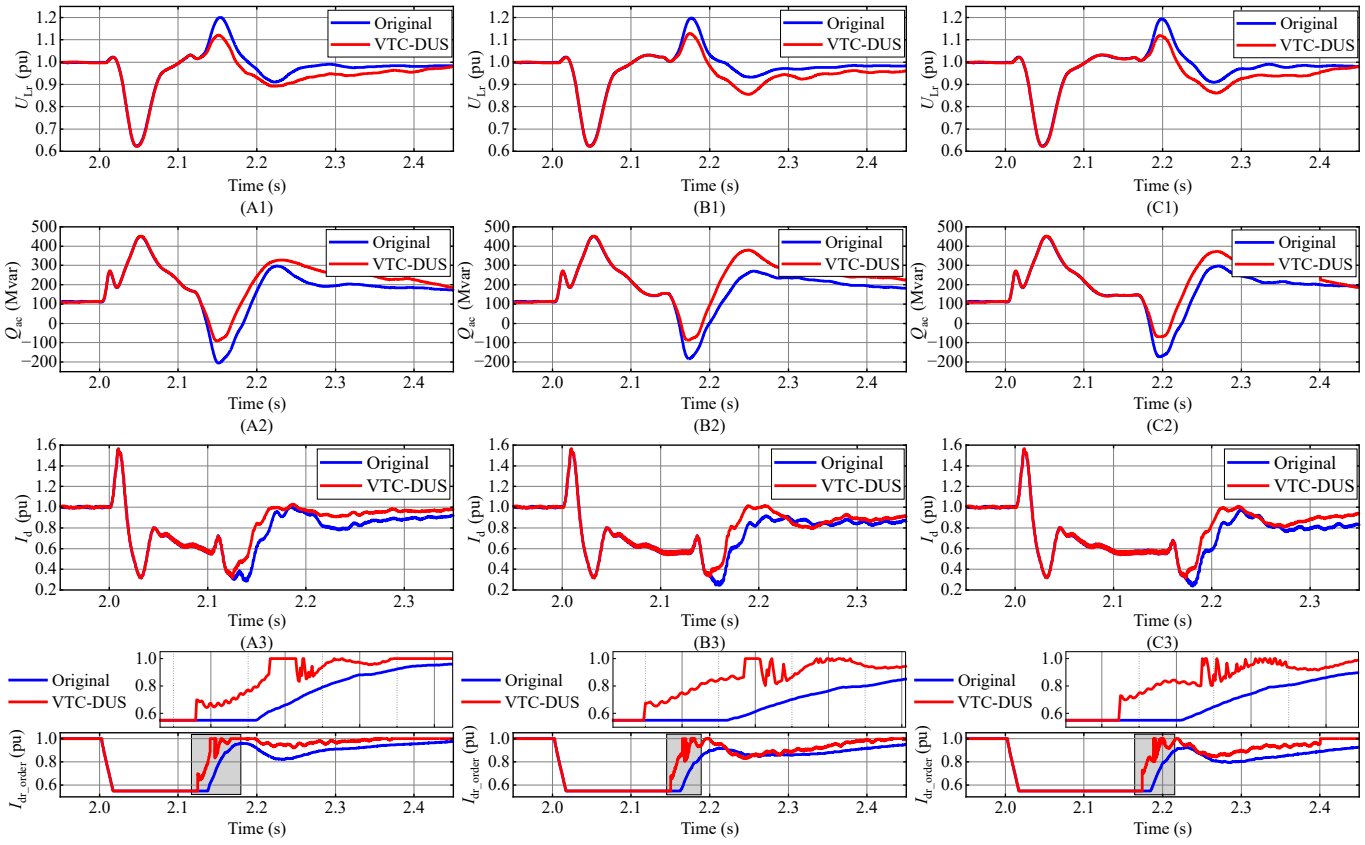

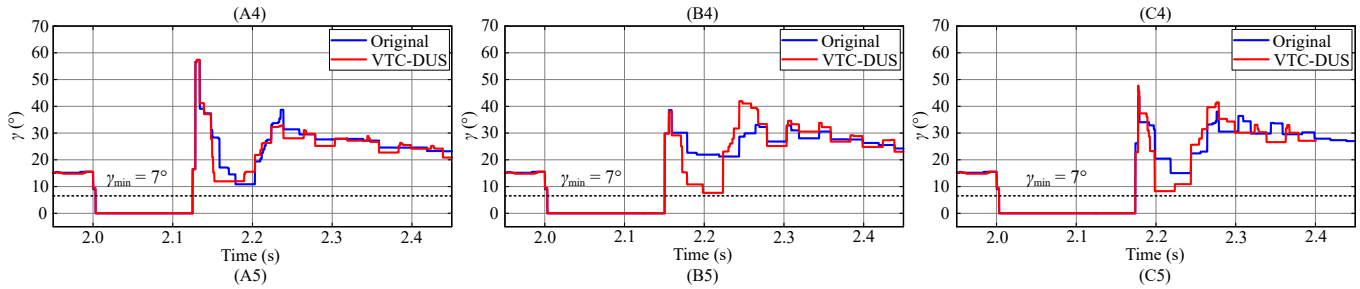

Fig. 13. Simulation results under different fault durations. Case A (A1–A5): TPG fault, L_f = 0.001 H, t_f = 0.1 s. Case B (B1–B5): TPG fault, L_f = 0.001 H, t_f = 0.125 s. Case C (C1–C5): TPG fault, L_f = 0.001 H, t_f = 0.15 s.

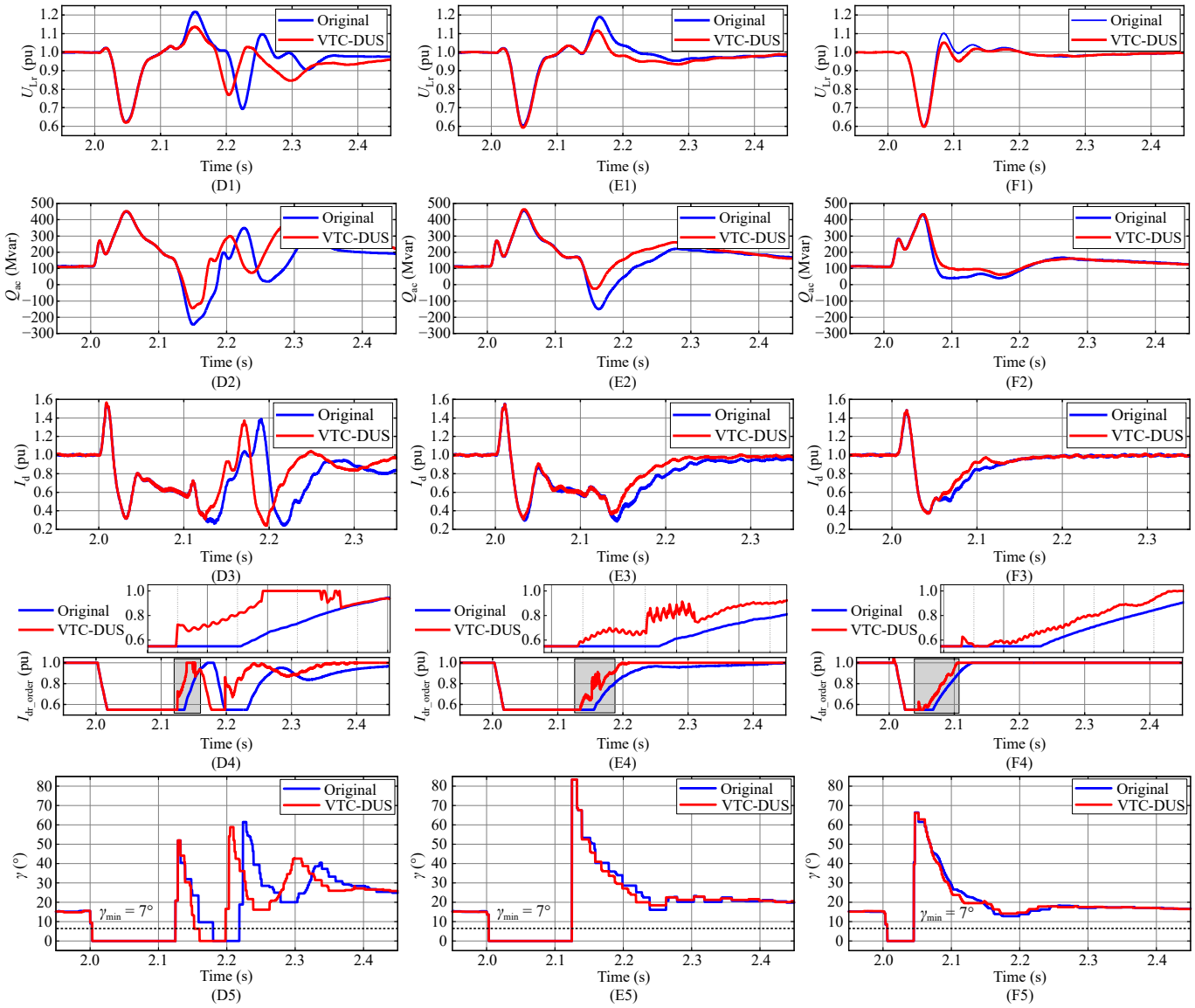

Fig. 14. Simulation results under different fault inductances. Case D (D1–D5): TPG fault, L_f = 0.0001 H, t_f = 0.1 s. Case E (E1–E5): TPG fault, L_f = 0.01 H, t_f = 0.1 s. Case F (F1–F5): TPG fault, L_f = 1 H, t_f = 0.1 s.

and individual valve currents in Figs. 16–18 are used to identify CFs and RCFs from the valve-current transfer process. The commutation state is therefore examined using both the extinction-angle response and the direct current-based criteria. Since VTC-DUS mainly acts during post-fault recovery rather than at fault inception, similar initial commutation responses

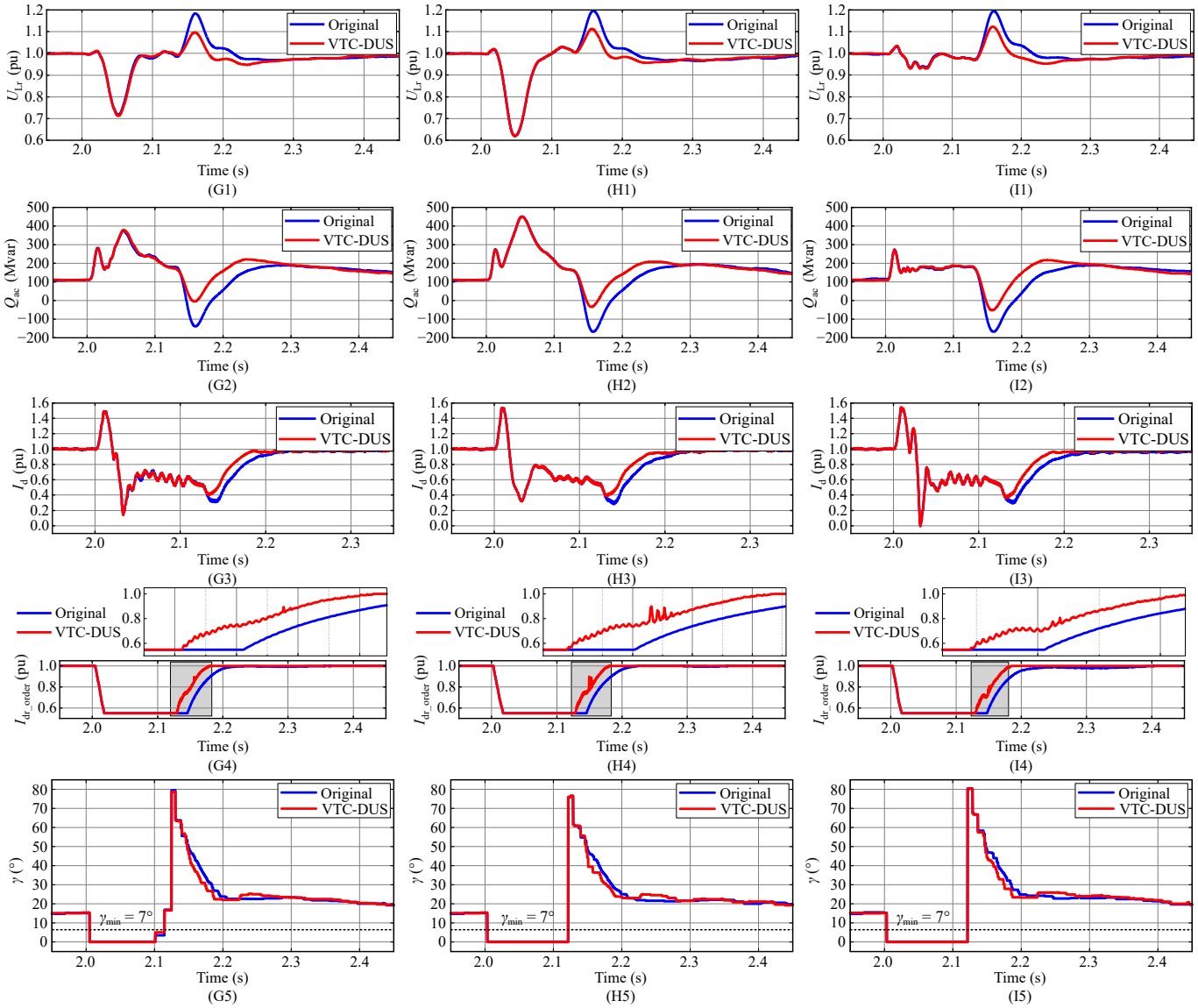

Fig. 15. Simulation results under different fault types (SPG fault, LLG fault, and LL fault). Case G (G1–G5): SPG fault, L_f = 0.001 H, t_f = 0.1 s. Case H (H1–H5): LLG fault, L_f = 0.001 H, t_f = 0.1 s. Case I (I1–I5): LL fault, L_f = 0.001 H, t_f = 0.1 s.

under the two control methods are expected. Therefore, the effectiveness of VTC-DUS is evaluated primarily from the post-fault TOV peak, DC-current undershoot, DC current order recovery, and RCF behavior, which are quantitatively summarized in Table 4.

Figure 13 shows the simulation waveforms under a three-phase-to-ground fault at the receiving-end AC bus (L_f = 0.001 H), with fault durations of 0.1 (case A), 0.125 (case B), and 0.15 s (case C). As shown by the simulation waveforms of the sending-end bus voltage U_{Lr} (A1, B1, and C1), the proposed strategy exhibits effective TOV suppression under different fault durations. As shown by the simulation waveforms of the DC current order I_{dr_order} (A4, B4, and C4), the DC current enters the recovery stage earlier, and the current order under the same voltage level is moderately elevated, thereby suppressing the excessive current drop (A3, B3, and C3). This ultimately reduces the reactive power exchange between the sending-end AC system and the rectifier station (A2, B2, and C2), effectively suppressing the TOV. Fig. 16 presents the current-based verification for cases A–C. As the fault duration increases, the abnormal valve-side current interval becomes longer and normal valve conduction recovers later. The six valve currents directly confirm the incomplete valve-to-valve current transfer during commutation failure. The similar initial responses under the two control methods indicate that VTC-DUS mainly affects the post-fault recovery process.

Figure 14 shows the simulation waveforms under a three-phase-to-ground fault at the receiving-end AC bus, with a fault duration of t_f = 0.1 s and fault severities corresponding to inductances of L_f = 0.0001 H (case D), L_f = 0.01 H (case E), and L_f = 1 H (case F). Because of the difference in fault severity, the system may experience an RCF. Under the most severe

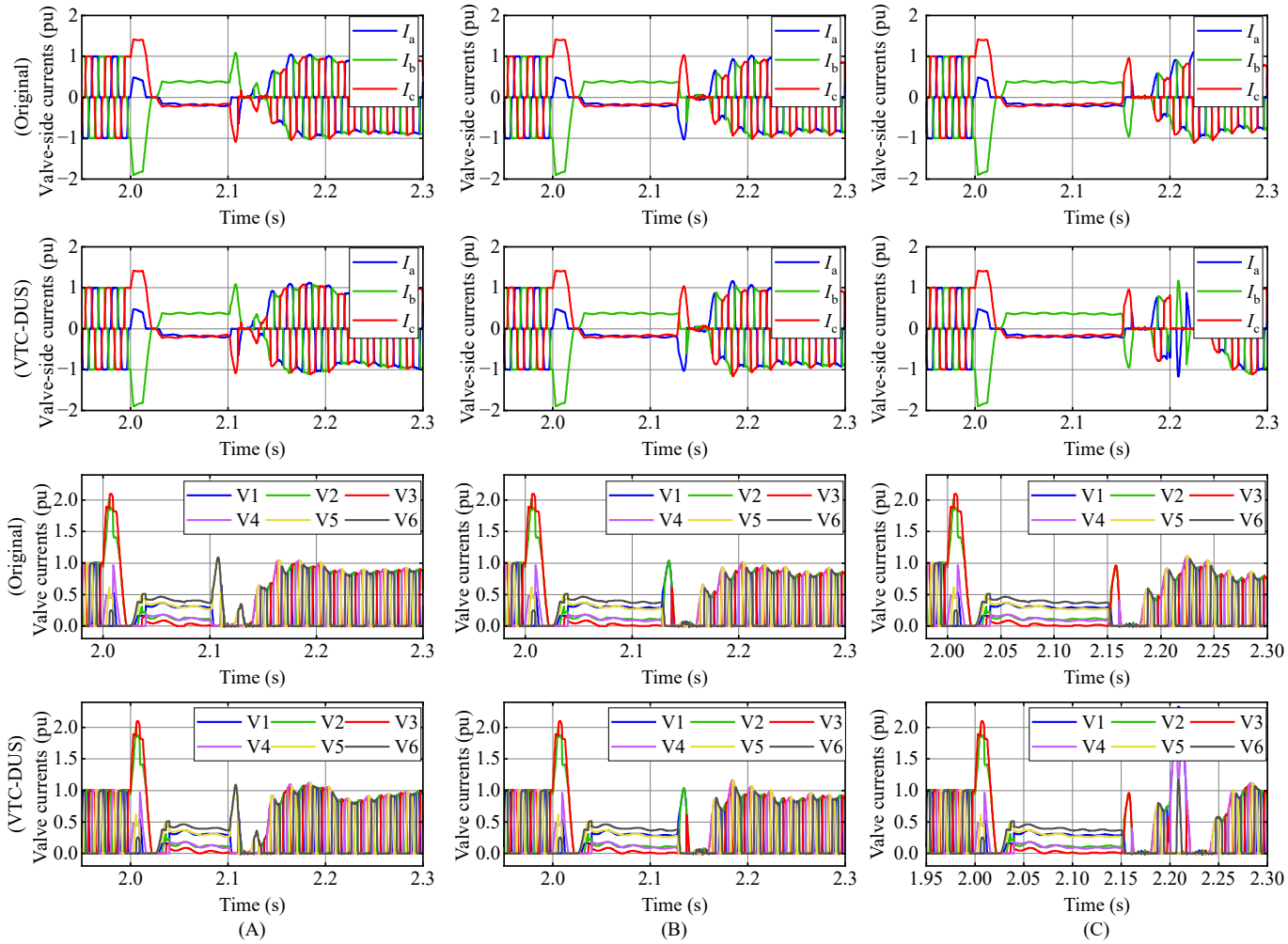

Fig. 16. Current-based verification of commutation failures under different fault durations. Columns 1–3 correspond to cases A–C, respectively. Rows 1 and 2 show the converter-transformer valve-side three-phase currents under the original control and VTC-DUS, respectively. Rows 3 and 4 show the corresponding six valve currents under the original control and VTC-DUS, respectively.

fault (case D), an RCF occurs with both the proposed strategy and the original control, and the sending-end bus voltage exhibits two TOV peaks (D1). Nevertheless, the proposed strategy still demonstrates good suppression performance. As the fault severity decreases, no RCF occurs. Under the mild fault (case F), the sending-end bus voltage peak does not exceed 1.1 pu (F1). In this case, the DC current calculation module in VTC-DUS is not activated (F4), and the suppression effect of the proposed strategy is correspondingly weakened. Figure 17 shows the corresponding results for cases D–F. With increasing fault inductance, the commutation disturbance becomes weaker and the valve currents recover more smoothly. The comparison confirms that VTC-DUS does not introduce additional abnormal commutation patterns relative to the original control. The valve-current waveforms also provide direct evidence for identifying the RCFs discussed above.

Figure 15 shows the simulation waveforms under different fault types with L_f = 0.001 H and fault duration t_f = 0.1 s, including an SPG fault (case G), an LLG fault (case H), and an LL fault (case I). As shown in Figs. 15(G1), (H1), and (I1), the proposed strategy effectively suppresses TOV under different fault types. Figure 18 presents the current-based verification under different asymmetric faults. The incomplete current-transfer process confirms the occurrence of commutation failure in cases G–I under both control methods.

To quantitatively evaluate the performance of VTC-DUS, the peak sending-end TOV, minimum DC current, DC current order recovery time, and occurrence of RCFs under cases A–I are summarized in Table 4. The TOV reduction ratio is defined based on the overvoltage component above 1.0 pu as

$$\eta_{\mathrm{TOV}} = \frac{U_{\mathrm{peak}}^{\mathrm{ori}} - U_{\mathrm{peak}}^{\mathrm{VTC}}}{U_{\mathrm{peak}}^{\mathrm{ori}} - 1} \times 100\% \tag{30}$$

The DC current order recovery time, τ_{ord}, is defined as the interval from fault inception to the instant at which the DC current order leaves its minimum plateau and begins sustained recovery. Because the fault is applied at $t_{\mathrm{f,on}}$ = 2.0 s in all cases, τ_{ord} is calculated as $\tau_{\mathrm{ord}} = t_{\mathrm{ord,rec}} - t_{\mathrm{f,on}}$.

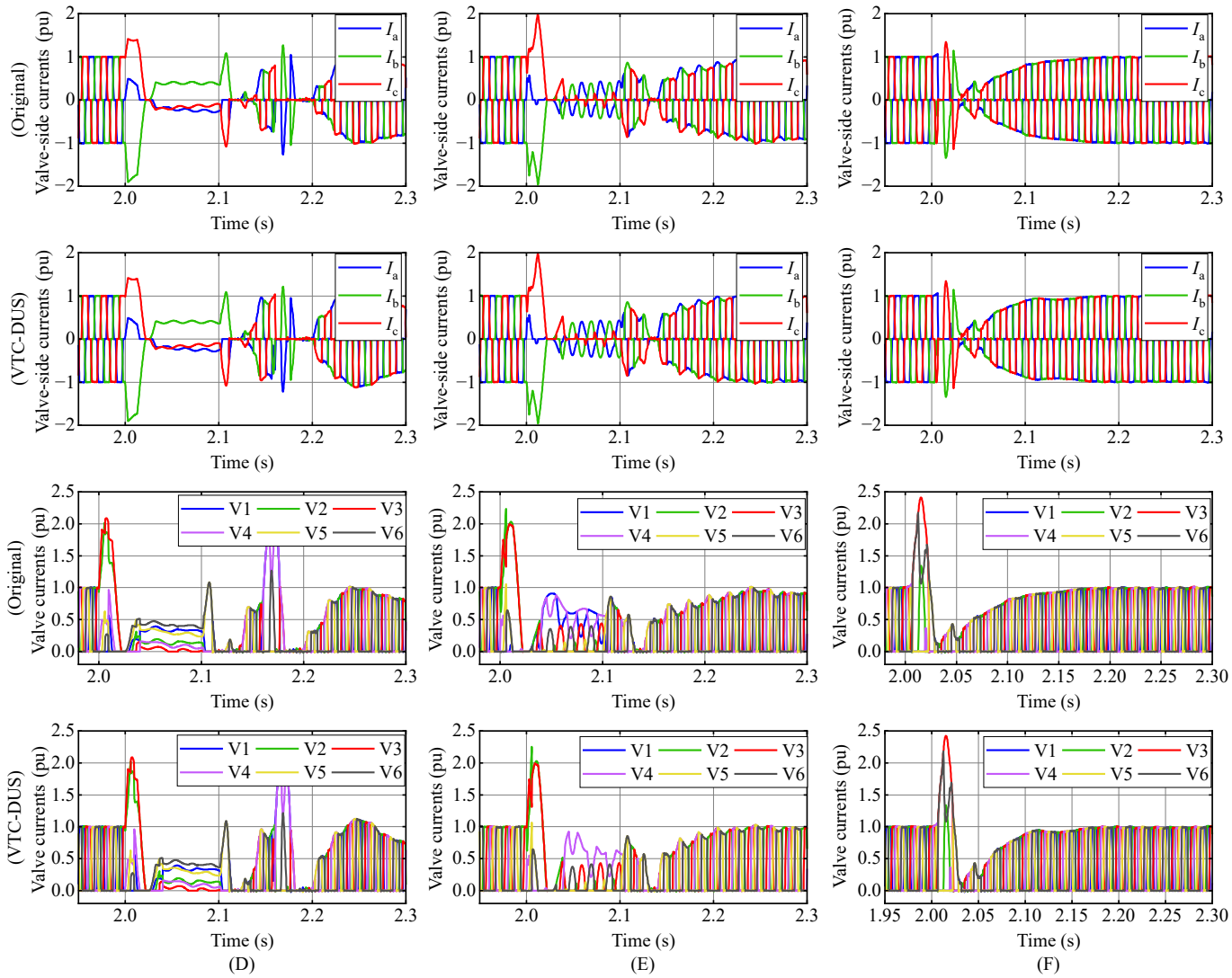

Fig. 17. Current-based verification of commutation failures under different fault inductances. Columns 1–3 correspond to cases D–F, respectively. Rows 1 and 2 show the converter-transformer valve-side three-phase currents under the original control and VTC-DUS, respectively. Rows 3 and 4 show the corresponding six valve currents under the original control and VTC-DUS, respectively.

As shown in Table 4, VTC-DUS reduces the absolute TOV peak by 0.050–0.088 pu under cases A–I. Relative to the overvoltage component above 1.0 pu, the corresponding TOV reduction ratios range from 34.8% to 49.5%. Meanwhile, the minimum DC current is increased by 0.003–0.103 pu, confirming that the excessive current undershoot is mitigated under all investigated conditions.

The DC current order recovery begins 11–23 ms earlier with VTC-DUS than with the original control. Only case D exhibits an RCF, and the RCF occurs under both control methods. Therefore, VTC-DUS does not introduce additional RCFs while improving the TOV and DC-current recovery characteristics under the investigated fault conditions.

C. Sensitivity analysis of the voltage threshold setting

To further demonstrate the flexible controllability of the proposed VTC-DUS, a sensitivity analysis with respect to the preset voltage threshold is carried out. Three threshold settings, $U_{\mathrm{Lr,max}}$ = 1.10, 1.12, and 1.15 pu, are considered. The corresponding sending-end voltage, DC current, and DC current order are shown in Fig. 19.

As shown in Fig. 19(a), the TOV peak follows the preset threshold level. When the voltage threshold is tightened from 1.15 to 1.10 pu, the peak value of the sending-end transient overvoltage is correspondingly reduced. This indicates that the proposed strategy can regulate the TOV level according to the prescribed voltage limit. Figure 19(c) shows that a lower voltage threshold causes the modified DC current order to leave the minimum plateau earlier and enter the recovery stage sooner. As a result, the actual DC current in Fig. 19(b) also starts recovering earlier. Therefore, the proposed strategy not only suppresses the TOV peak, but also provides a controllable recovery trajectory of the DC current through the threshold setting. These results verify that the proposed VTC-DUS

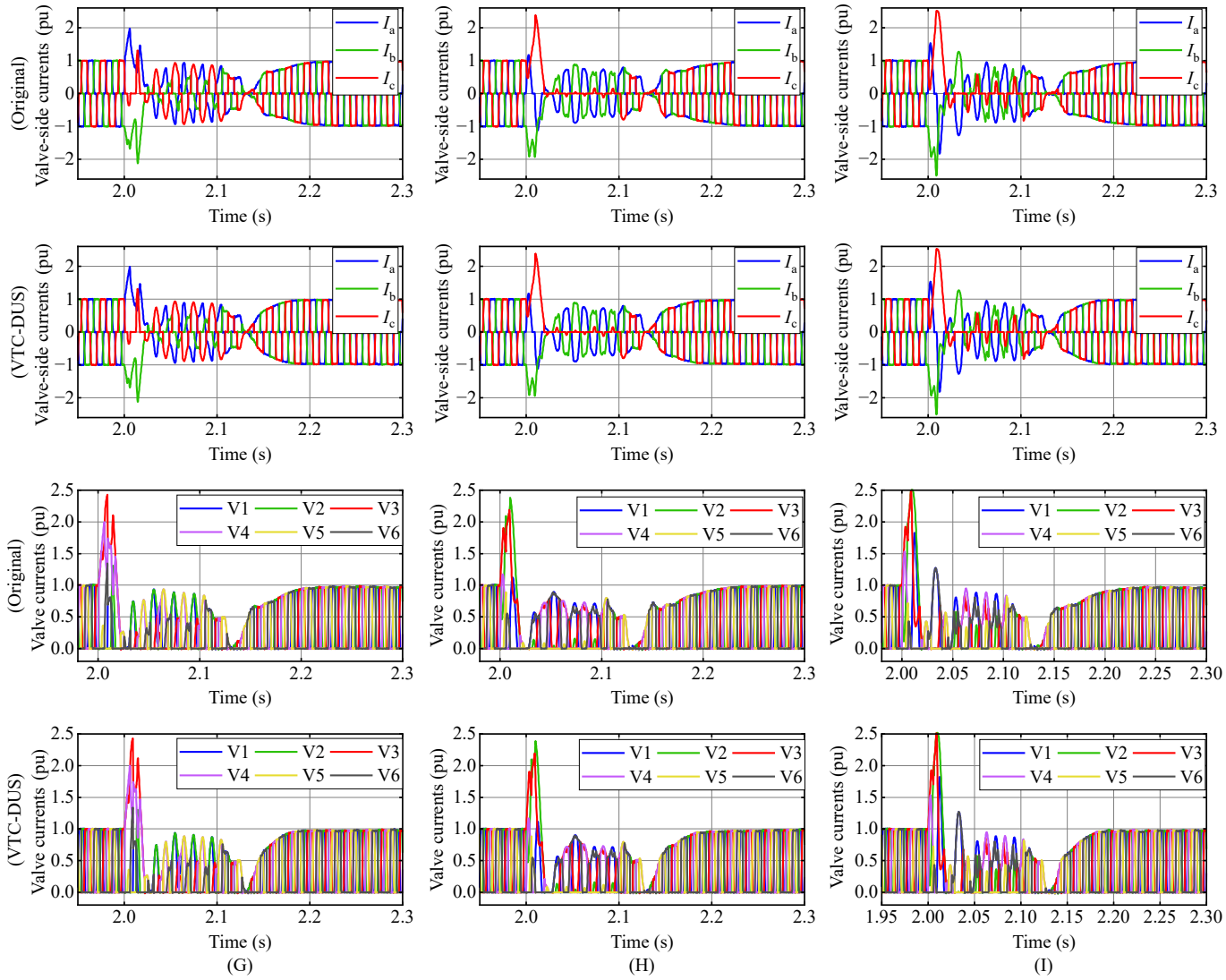

Fig. 18. Current-based verification of commutation failures under different fault types. Columns 1–3 correspond to cases G–I, respectively. Rows 1 and 2 show the converter-transformer valve-side three-phase currents under the original control and VTC-DUS, respectively. Rows 3 and 4 show the corresponding six valve currents under the original control and VTC-DUS, respectively.

TABLE 4
QUANTITATIVE COMPARISON BETWEEN THE ORIGINAL CONTROL AND VTC-DUS UNDER DIFFERENT FAULT CONDITIONS

Case	Strategy	Peak TOV (pu)	TOV reduction ratio η_{TOV} (%)	Minimum DC current (pu)	Current-order recovery time τ_{ord} (s)	RCF
A	Original	1.200	—	0.282	0.138	No
A	VTC-DUS	1.121	39.5	0.318	0.125	No
B	Original	1.198	—	0.244	0.163	No
B	VTC-DUS	1.129	34.8	0.342	0.151	No
C	Original	1.194	—	0.241	0.185	No
C	VTC-DUS	1.119	38.7	0.314	0.174	No
D	Original	1.217	—	0.261	0.136	Yes
D	VTC-DUS	1.135	37.8	0.328	0.125	Yes
E	Original	1.189	—	0.283	0.155	No
E	VTC-DUS	1.116	38.6	0.365	0.135	No
F	Original	1.101	—	0.369	0.068	No

TABLE 4
QUANTITATIVE COMPARISON BETWEEN THE ORIGINAL CONTROL AND VTC-DUS UNDER DIFFERENT FAULT CONDITIONS (CONTINUED)

Case	Strategy	Peak TOV (pu)	TOV reduction ratio η_{TOV} (%)	Minimum DC current (pu)	Current-order recovery time τ_{ord} (s)	RCF
F	VTC-DUS	1.051	49.5	0.372	0.045	No
G	Original	1.184	—	0.307	0.146	No
G	VTC-DUS	1.096	47.8	0.402	0.130	No
H	Original	1.195	—	0.282	0.145	No
H	VTC-DUS	1.112	42.6	0.385	0.129	No
I	Original	1.195	—	0.289	0.148	No
I	VTC-DUS	1.123	36.9	0.359	0.130	No

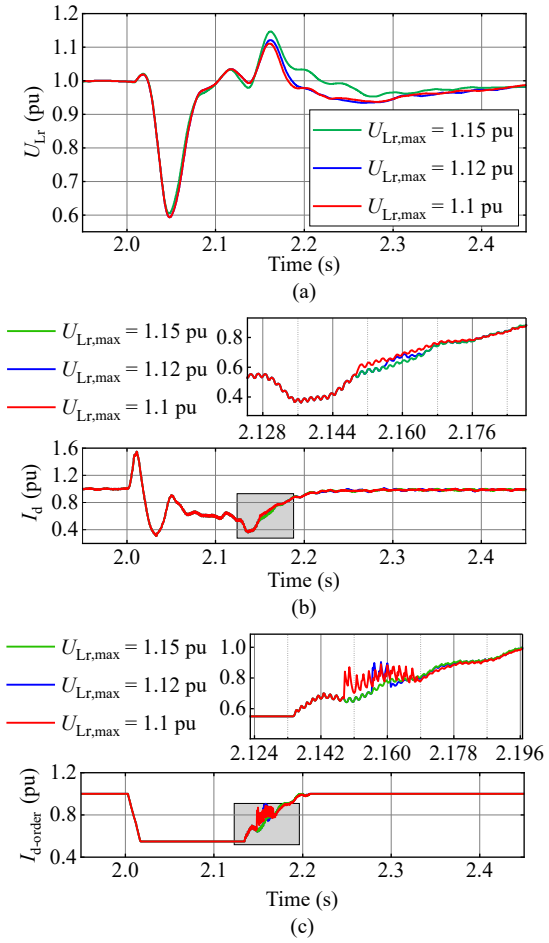

Fig. 19. Sensitivity analysis of the preset voltage threshold in VTC-DUS. (a) Sending-end bus voltage under different threshold settings. (b) DC current under different threshold settings. (c) DC current order under different threshold settings.

achieves flexible and effective suppression of the sending-end TOV under different threshold settings.

6. CONCLUSIONS

This paper addresses the issue of sending-end transient overvoltage in a wind power integrated LCC-HVDC system under commutation failure, and draws the following main conclusions:

(1) During the recovery period following CFs, the excessive drop in DC current is identified as a major aggravating factor for sending-end TOV under the studied conditions. The overaction of the rectifier-side CCC induces an undershoot effect, which leads to an excessive current reduction. This reduction decreases the reactive power absorbed by the rectifier station, thereby becoming a crucial factor that exacerbates the TOV.

(2) The proposed TOV assessment method that incorporates the dynamic reactive power response of the wind farm has a peak error of less than 0.01 pu under TPG faults and less than 0.03 pu under SPG faults. Its accuracy is significantly better than that of simplified models that neglect either the dynamic reactive-power response of the wind farm or the transient variation of the DC voltage. The slightly larger error under SPG faults is due to the non-ideal commutation characteristics under asymmetrical faults.

(3) The proposed VTC-DUS first employs the voltage evaluation method that accounts for the dynamic reactive power response of the wind farm to calculate a DC current lower limit constrained by a preset voltage threshold, thereby generating a modified order. Then, based on the deviation between the modified order and the actual current, it drives the adaptive shift of the VDCOL characteristic, so that the current order is moderately elevated while maintaining a gradual variation characteristic. Simulation results show that, under cases A–I, VTC-DUS reduces the absolute sending-end TOV peak by 0.050–0.088 pu, corresponding to a reduction of 34.8%–49.5% in the overvoltage component above 1.0 pu. The minimum DC current is increased by 0.003–0.103 pu, and the DC current-order recovery begins 11–23 ms earlier. Under extremely severe faults, although it cannot completely avoid RCFs, it can still reduce the TOV level. Sensitivity analysis confirms that the TOV suppression level and DC-current recovery trajectory can be flexibly regulated by adjusting $U_{Lr,max}$.

Declaration of competing interest

The authors declare that they have no known competing financial interests or personal relationships that could have appeared to influence the work reported in this paper.

Acknowledgements

This work is carried out without the support of any funding agency.

Use of AI statement

None.

REFERENCES

[1] S. Zhou, X. L. Yang, T. T. Lie, W. Y. Zhao, J. P. Han, and W. D. Shao, "International research progress and future trends of energy transition driven by climate change: a review," *Power Energy Future*, vol. 1, no. 1, pp. 9650003, Mar. 2026.

[2] A. C. Xue, L. Yue, J. H. Zhang, J. H. Cui, Z. Q. Li, Y. C. Li, L. Gao, W. F. Lin, and X. Y. Ren, "A new quantitative analysis method for overvoltage in sending end electric power system with UHVDC," *IEEE Access*, vol. 8, pp. 145898–145908, Aug. 2020.

[3] C. Y. Yin and F. T. Li, "Analytical expression on transient overvoltage peak value of converter bus caused by DC faults," *IEEE Trans. Power Syst.*, vol. 36, no. 3, pp. 2741–2744, May 2021.

[4] H. Xiao, X. Z. Duan, Y. Zhang, and Y. H. Li, "Analytically assessing the effect of strength on temporary overvoltage in hybrid multi-infeed HVdc systems," *IEEE Trans. Power Electron.*, vol. 37, no. 3, pp. 2480–2484, Mar. 2022.

[5] Q. Xie, Z. X. Zheng, Y. Wang, W. X. Hu, X. Y. Xiao, K. J. Du, and J. Ren, "Analysis of transient voltage disturbances in LCC-HVDC sending systems caused by commutation failures," *IEEE Trans. Power Deliv.*, vol. 37, no. 5, pp. 4370–4381, Oct. 2022.

[6] X. Y. Liu, H. H. Xin, D. Zheng, and B. Cao, "Temporary overvoltage assessment and suppression in heterogeneous renewable energy power systems," *Int. J. Electr. Power Energy Syst.*, vol. 155, pp. 109472, Jan. 2024.

[7] D. Liu, F. Y. Li, T. Q. Liu, S. Zhang, and S. Q. Jiang, "Quantitative calculation method and its overvoltage suppression strategy for sending-end transient voltage of LCC-HVDC under commutation failure," *Energy Rep.*, vol. 13, pp. 3418–3429, Jun. 2025.

[8] B. Wang, Z. Z. Li, X. C. He, Q. Yuan, and Y. Xia, "Calculation method for line-commutated converter HVDC transient response based on dynamic Phasor," *Electr. Power Syst. Res.*, vol. 248, pp. 111889, Nov. 2025.

[9] C. Y. Yin and F. T. Li, "Reactive power control strategy for inhibiting transient overvoltage caused by commutation failure," *IEEE Trans. Power Syst.*, vol. 36, no. 5, pp. 4764–4777, Sep. 2021.

[10] Q. Xie, X. Y. Xiao, Z. X. Zheng, Y. Wang, D. H. Song, K. J. Du, Y. Zou, and J. C. Zhang, "An improved reactive power control strategy for LCC-HVDC to mitigate sending end transient voltage disturbance caused by commutation failures," *Int. J. Electr. Power Energy Syst.*, vol. 146, pp. 108706, Mar. 2023.

[11] X. Jin and H. Nian, "Overvoltage suppression strategy for sending AC grid with high penetration of wind power in the LCC-HVdc system under commutation failure," *IEEE Trans. Power Electron.*, vol. 36, no. 9, pp. 10265–10277, Sep. 2021.

[12] C. Y. Yin and C. S. Su, "DC current prediction and suppression control strategies for inhibiting commutation failure in LCC-HVDC," *Electr. Power Syst. Res.*, vol. 220, pp. 109359, Jul. 2023.

[13] Y. Wang, J. H. Zhu, Y. B. Li, J. B. Hu, S. C. Ma, and T. Z. Wang, "Transient overvoltage suppression of LCC-HVDC sending-end system based on DC current control optimisation," *IET Energy Syst. Integr.*, vol. 6, no. 2, pp. 182–195, Jun. 2024.

[14] B. Pang, Y. Tang, Q. W. Zhang, K. Liao, J. W. Yang, S. Lin, and Z. Y. He, "A multi-stage DC current control strategy for suppressing transient overvoltage of LCC-HVDC sending end grid," *Int. J. Electr. Power Energy Syst.*, vol. 173, pp. 111232, Dec. 2025.

[15] W. Liu, C. Y. Yin, and F. T. Li, "A novel control strategy for suppression of transient overvoltage and subsequent commutation failure for LCC-HVDC," *IEEE Trans. Power Deliv.*, vol. 40, no. 6, pp. 3542–3553, Dec. 2025.

[16] Manitoba Hydro International Ltd., "Type 3 wind turbine model," Manitoba Hydro International Ltd., Winnipeg, Manitoba, PSCAD X4 version 4.6, Nov. 2018.

[17] A. Y. Goharrizi, J. C. Garcia Alonso, E. Borisova, F. Mosallat, and D. Muthumuni, "Benchmark model of type-III wind turbine for research and development applications," in *Proceedings of 2018 IEEE Canadian Conference on Electrical & Computer Engineering*, 2018, pp. 1–6.

[18] J. Z. Tu, Y. Pan, J. Zhang, B. Zeng, J. C. Jia, and J. Yi, "Transient reactive power characteristics of HVDC during commutation failure and impact of HVDC control parameters," *J. Eng.*, vol. 2017, no. 13, pp. 1134–1139, Dec. 2017.

[19] M. P. Bahrman and B. K. Johnson, "The ABCs of HVDC transmission technologies," *IEEE Power Energy Mag.*, vol. 5, no. 2, pp. 32–44, Mar./Apr. 2007.



He Wang, Professor, Doctoral Supervisor. His research interests include flexible DC transmission, renewable energy generation, and power system communication.

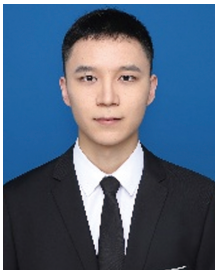

Han Zhang, Master's candidate. His main research interests include LCC-HVDC systems, mechanism analysis and suppression of sending-end transient overvoltage under commutation failures, and DC current control strategies.

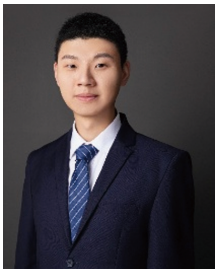

Jiajun Ma received his M.Sc. degree with Merit and Ph.D. degree in Electronic and Electrical Engineering from the University of Strathclyde, United Kingdom. He is currently with the Department of Electronic and Electrical Engineering at the University of Strathclyde. His research focuses on power system stability and security analysis, probabilistic power flow, harmonic power flow, distribution network operation, and the modelling of power systems with high levels of converter-interfaced generation.



Jing Bian, Associate Professor, Master's Supervisor. His research focuses on the modeling and simulation of flexible DC transmission systems.



Jiazhi Guo, Ph.D. candidate. His main research interest is the modeling and simulation of flexible DC transmission systems.